Inferring geostatistical properties of hydraulic conductivity fields from saline tracer tests and equivalent electrical conductivity time-series

Alejandro Fernandez Visentini [a,*], Niklas Linde [a], Tanguy Le Borgne [b], Marco Dentz [c]

[a] *Institute of Earth Sciences, University of Lausanne, Lausanne CH-1015, Switzerland*
[b] *Université de Rennes 1, CNRS, Géosciences Rennes UMR 6118, Rennes 35042, France*
[c] *IDAEA-CSIC, Jordi Girona 18-26, Barcelona 08034, Spain*

ABSTRACT

We use Approximate Bayesian Computation and the Kullback–Leibler divergence measure to quantify to what extent horizontal and vertical equivalent electrical conductivity time-series observed during tracer tests constrain the 2-D geostatistical parameters of multivariate Gaussian log-hydraulic conductivity fields. Considering a perfect and known relationship between salinity and electrical conductivity at the point scale, we find that the horizontal equivalent electrical conductivity time-series best constrain the geostatistical properties. The variance, controlling the spreading rate of the solute, is the best constrained geostatistical parameter, followed by the integral scales in the vertical direction. We find that horizontally layered models with moderate to high variance have the best resolved parameters. Since the salinity field at the averaging scale (e.g., the model resolution in tomograms) is typically non-ergodic, our results serve as a starting point for quantifying uncertainty due to small-scale heterogeneity in laboratory-experiments, tomographic results and hydrogeophysical inversions involving DC data.

1. Introduction

Time-lapse electrical geophysical methods are popular in hydrogeology (e.g., Binley et al., 2015; Singha et al., 2015) as they provide non-intrusive means for remote and dense spatio-temporal sampling related to flow and transport processes. Among these, the direct-current (DC) method is cost-effective, easy to employ and probably the most commonly used (Binley et al., 2015). It has been thoroughly assessed through numerical investigations (e.g., Vanderborght et al., 2005; Singha and Gorelick, 2005; Fowler and Moysey, 2011), laboratory and controlled tank experiments (Slater et al., 2000; Koestel et al., 2008; Jougnot et al., 2018), and field investigations (e.g., Daily et al., 1992; Binley et al., 2002; Singha and Gorelick, 2005).

DC measurements are generally based on two pairs of electrodes: one pair for establishing a known electrical current between two points, and the other for measuring the resultant electrical voltage between two other points (e.g., Keller and Frischknecht, 1966). In the context of time-lapse DC tomographic experiments, the measurement process is repeated using multiple current and voltage electrode pairs at different positions, and the measurement protocol is repeated over time. Such a measurement process is often referred to as time-lapse Electrical Resistivity Tomography (ERT), and it outputs time-series of electrical resistances (voltage over injected current) that in saturated media carry information about the time-evolution of the salinity distribu-

tion (e.g., Lesmes and Friedman, 2005). The time-lapse ERT method has been applied during conservative saline tracer tests to extract both flow and transport information. Retrieval of hydraulic conductivity from such data is discussed, for example, in Kemna et al. (2002) and Vanderborght et al. (2005) and the range of applications span from the calibration of mean hydraulic conductivity values (Binley et al., 2002) to retrieval of the full distribution of hydraulic conductivity (Pollock and Cirpka, 2012). Extraction of solute transport parameters has been studied in detail and (Kemna et al., 2002), for instance, provided a field demonstration of retrieving equivalent 1-D stream-tube advective-dispersive transport parameters in the context of 3-D conservative saline transport, results later corroborated numerically by Vanderborght et al. (2005). Also (Koestel et al., 2008) inferred the 3-D distribution of solute velocities and dispersivities in a soil column using time-lapse ERT data.

Over time, the use of geoelectrical-monitored tracer tests has evolved from qualitative analyses such as saline plume motion detection and geometry delineation (e.g., Slater et al., 2000) to obtain quantitative and spatially-resolved hydrological constraints. Nevertheless, using time-lapse DC data for quantitative hydrogeological purposes remains a persistent challenge (Singha et al., 2015). This challenge is intimately related to the use of time-lapse inversion methodologies that provide resolution-limited time-evolving images of electrical resistivity or conductivity through time (Singha et al., 2015). The most common approach to translate resulting geophysical time-lapse tomograms

---

into salinity distributions rests on two strong assumptions. The first is that there exists a petrophysical relationship, (e.g., Archie, 1942), with known spatially-invariant parameters defined at the discretization scale of the tomogram, implying that it corresponds to the Representative Elementary Volume (REV) scale (Hill, 1963) of bulk electrical conductivity and, consequently, that the impact of salinity heterogeneity is negligible below this scale. The second assumption is that the resolution of the geophysical tomogram is the same as the model discretization, which is hardly true for any electrical survey. In reality, the tomogram represents spatially-varying weighted averages over a much larger volume (e.g., Friedel, 2003). With these two assumptions, temporal differences in time-lapse tomograms can readily be translated into estimates of salinity differences. Unfortunately, this approach typically leads to an underestimation of actual tracer mass with errors often approaching one order of magnitude (e.g., Binley et al., 2002; Singha and Gorelick, 2005; Laloy et al., 2012). Research has addressed the second assumption by upscaling the petrophysical relationship to the tomographic resolution using either linearized inverse theory (Day-Lewis et al., 2005; Nussbaumer et al., 2019) or Monte Carlo-based simulation approaches (e.g., Moysey et al., 2005).

In this work, we are primarily concerned with the first assumption, namely that the impact of salinity variations is negligible below a given scale. To avoid complications inherent to tomographic imaging, we focus here on the case of a time-evolving equivalent electrical conductivity tensor of a 2-D square sample of unit length that is invaded by a saline (i.e., electrically conductive) tracer. In a tomographic setting, this scale can be thought of as the model resolution at a given location of interest. For this case, the equivalent electrical conductivity in a given direction is readily obtained, basically by dividing the electric current with the imposed voltage. The total current is the macroscopic flux of the internal current density field (i.e., the distribution of small-scale currents within the sample) that, for a given internal distribution of local conductivities, is established such that its associated energy loss due to Joule's dissipation, integrated over the domain, is minimized (e.g., Feynman et al., 2011; Bernabé and Revil, 1995). This governing principle leads to patterns of current channelling and deflection through and from high and low electrical conductivity zones, respectively, and it governs the time variations of the current density field as the saline tracer invades the sample (e.g., Li and Oldenburg, 1991). Accurate prediction of the time-evolution of the equivalent electrical conductivity of the medium, thus, requires accounting for interactions occurring throughout the domain and, given an arbitrarily-shaped time-evolving electrical conductivity field, this remains an open upscaling problem belonging to the family of conductivity upscaling in spatially non-stationary fields (e.g., Sanchez-Vila et al., 2006 and references therein). The current lack of physically accurate upscaling procedures impedes reliable quantitative analyses of a saline plume's fate from geoelectrical monitoring. For instance, in the most common case where Archie's petrophysical law (Archie, 1942) is used to infer the mean saline concentration within the sample from its equivalent electrical conductivity, the underlying assumption is that the internal electrical conductivity field behaves as an additive property that can be upscaled by taking its arithmetic average. This is only true if the electrical conductivity field is constant or if its distribution is layered and the equivalent electrical conductivity is measured parallel to this layering, corresponding to the upper Wiener bound (e.g., Milton and Sawicki, 2003). In general, since portions of the concentration field are by-passed by the established current patterns, the upper Wienner bound does not apply and this leads to the above-mentioned apparent mass loss as demonstrated, for example, in a recent laboratory study (Jougnot et al., 2018). These issues also impact the performance of many fully-coupled hydrogeophysical inversion approaches and modeling studies that interpret equivalent electrical conductivity time-series using equivalent transport parameters within an advective-dispersive description (e.g., Kemna et al., 2002; Vanderborght et al., 2005; Koestel et al., 2008). On a more positive note, the discussion above also suggests

that electrical conductivity time-series at a given scale carry statistical information on the concentration field and its temporal evolution.

Here we investigate to what extent tracer tests associated with time-series of equivalent electrical properties a pre-defined scale can be used to infer geostatistical properties of hydraulic conductivity fields below this scale. This is achieved by considering inference within a Bayesian inference framework (e.g., Gelman et al., 2013; Tarantola, 2005), more specifically through an Approximate Bayesian Computational approach (e.g., Beaumont et al., 2002; Sisson et al., 2018). For comparison purposes, the mass breakthrough curve is also evaluated and its information content is compared to its electrical peers. Using a Bayesian approach allows assessing the information gained on the properties of interest with respect to their assumed prior statistics. We perform our study using a database consisting of 10^5 synthetically-generated equivalent electrical conductivity tensor and mass breakthrough time-series collected during saline tracer tests within a 2-D domain with hydraulic heterogeneity prescribed by multivariate Gaussian fields. We consider advectively-dominated solute transport (i.e., high Péclet numbers), where the concentration field evolution is predominantly determined by the underlying flow field, which in turn depends on the underlying hydraulic conductivity field under the constant applied pressure gradient. In this study, we consider idealized scenarios as it is assumed that there is no spatial variations in petrophysical properties and that the petrophysical relationship is known.

In Section 2 we review the basic governing equations describing groundwater flow, solute transport and electrical conduction together with their numerical implementations. In Section 3 we introduce the inference problem of interest along with the Bayesian inference tools. The main results are presented and discussed in Sections 4 and 5, respectively. Section 6 concludes the paper.

2. Governing equations and problem setup

2.1. Groundwater flow

For steady-state flow and in the absence of sources or sinks, mass conservation of an incompressible fluid is expressed by the continuity equation for the specific discharge $\mathbf{q}(\mathbf{x})$:

$$\nabla.\mathbf{q}(\mathbf{x}) = 0, \tag{1}$$

where $\mathbf{x} = (x, y)^T$ denotes the 2-D position vector and x and y the horizontal and vertical coordinates, respectively. Darcy's law relates $\mathbf{q}(\mathbf{x})$ with the hydraulic conductivity field $K(\mathbf{x})$ and the hydraulic head $h(\mathbf{x})$ via

$$\mathbf{q}(\mathbf{x}) = -K(\mathbf{x})\nabla h(\mathbf{x}). \tag{2}$$

Adopting Darcy's law, the groundwater flow equation reads:

$$\nabla K(\mathbf{x})\nabla h(\mathbf{x}) + K(\mathbf{x})\nabla^2 h(\mathbf{x}) = 0. \tag{3}$$

It is customary to treat the log-hydraulic conductivity field $Y(\mathbf{x})$ ($\equiv \ln(K(\mathbf{x}))$) within a geostatistical framework with $Y(\mathbf{x})$ modelled as a second-order spatially-stationary ergodic random function. In this study, we consider multivariate-Gaussian random fields with an exponential covariance structure (e.g., Rubin, 2003) with a mean μ_Y and a variance σ_Y^2. The integral scales of the field are expressed by the integral scale I_y in the vertical direction and an anisotropy factor λ ($= I_x/I_y$). After specifying $K(\mathbf{x})$, the flow field $\mathbf{q}(\mathbf{x})$ is obtained by solving Eq. (3) with prescribed boundary conditions (Section 2.4.2).

2.2. Solute transport

The evolution of the concentration field $c(\mathbf{x}, t)$ of a passive tracer being transported within the steady-state flow-field $\mathbf{q}(\mathbf{x})$ can be described within an Eulerian framework using the advection-dispersion equation

$$\theta \frac{\partial c(\mathbf{x}, t)}{\partial t} + \nabla.[(\mathbf{q}(\mathbf{x})c(\mathbf{x}, t) - \theta\mathbf{D}\nabla c(\mathbf{x}, t)] = 0, \tag{4}$$

where θ is the porosity and $\mathbf{D}$ is the dispersion tensor. In this study we assume a spatially-constant porosity and dispersion tensor, and furthermore we assume zero dispersivity. In this case and considering Eq. (1), Eq. (4) simplifies to the advection-diffusion equation with constant coefficients:

$$\theta \frac{\partial c}{\partial t} + \mathbf{q}(\mathbf{x}).\nabla c - \theta D_m \nabla^2 c = 0, \tag{5}$$

where D_m denotes the molecular diffusion coefficient. After solving for $c(\mathbf{x}, t)$, the flux-weighted tracer mass-breakthrough time-series $M(t)$ are defined by

$$M(t) = \frac{\int_{\Gamma_{out}} q_x(\mathbf{x}) c(\mathbf{x}, t) d\mathbf{x}}{\int_{\Gamma_{out}} q_x(\mathbf{x}) d\mathbf{x}}, \tag{6}$$

with $q_x(\mathbf{x})$ being the flow-component in the x-direction and Γ_{out} the outflow boundary of the model domain.

2.3. DC conduction

Electric charge conservation is in the DC problem expressed by the continuity equation of the current density field $\mathbf{J}(\mathbf{x,t})$ at time-lapse acquisition time t. In the absence of current sources and net accumulation of electric charge, it takes the following form:

$$\nabla.\mathbf{J}(\mathbf{x}, t) = 0. \tag{7}$$

Ohm's law relates $\mathbf{J}(\mathbf{x}, t)$ with the electrical conductivity $\sigma(\mathbf{x}, t)$ and the electric field $\mathbf{E}(\mathbf{x}, t)$ via the linear relationship $\mathbf{J}(\mathbf{x}, t) = \sigma(\mathbf{x}, t)\mathbf{E}(\mathbf{x}, t)$. Adopting the quasistatic approximation, $\nabla \times \mathbf{E}(\mathbf{x}, t) = 0$, allows to express $\mathbf{E}(\mathbf{x}, t) = -\nabla \phi(\mathbf{x}, t)$, where $\phi(\mathbf{x}, t)$ is the electrical potential. Writing $\mathbf{J}(\mathbf{x}, t)$ in terms of $\phi(\mathbf{x}, t)$ as $\mathbf{J}(\mathbf{x}, t) = -\sigma(\mathbf{x}, t)\nabla \phi(\mathbf{x}, t)$ and replacing this expression into Eq. (7) results in the governing Laplace equation for the electrical potentials:

$$\nabla \sigma(\mathbf{x}, t)\nabla \phi(\mathbf{x}, t) + \sigma(\mathbf{x}, t)\nabla^2 \phi(\mathbf{x}, t) = 0. \tag{8}$$

We consider the horizontal and vertical components of the equivalent electrical conductivity tensor time-series of a 2-D square sample of unit length. This implies solving Eq. (8) with alternative mixed Dirichlet–Neumann boundary conditions or "excitation modes". For $\sigma^H(t)$ ($\sigma^V(t)$), a constant electrical potential difference $\Delta \phi_H$ ($\Delta \phi_V$) along the horizontal (vertical) direction is imposed, with zero electrical potential gradient along the top and bottom (left and right) boundaries. The resulting electrical potential fields are, respectively, $\phi^H(\mathbf{x}, t)$ and $\phi^V(\mathbf{x}, t)$. The corresponding equivalent electrical conductivity time-series are computed as

$$\sigma^H(t) = \frac{1}{\Delta \phi_H} \int_{\Gamma_y} -\sigma(\mathbf{x}, t)\nabla_x \phi^H(\mathbf{x}, t) d\mathbf{x}, \tag{9}$$

and

$$\sigma^V(t) = \frac{1}{\Delta \phi_V} \int_{\Gamma_x} -\sigma(\mathbf{x}, t)\nabla_y \phi^V(\mathbf{x}, t) d\mathbf{x}, \tag{10}$$

where the integration paths Γ_y and Γ_x are any two given contours separating the left and right boundaries and the top and bottom boundaries, respectively, and the integrands in each equation is the horizontal or vertical component of the current density field resulting from each excitation mode.

2.4. Numerical implementations and problem setup

We create a database of 10^5 time-series of $\sigma^H(t)$, $\sigma^V(t)$ and $M(t)$ that are collected during tracer tests simulated within multivariate Gaussian log-hydraulic conductivity realizations in a square-shaped domain of side length $L = 1$ m discretized into 250×250 elements.
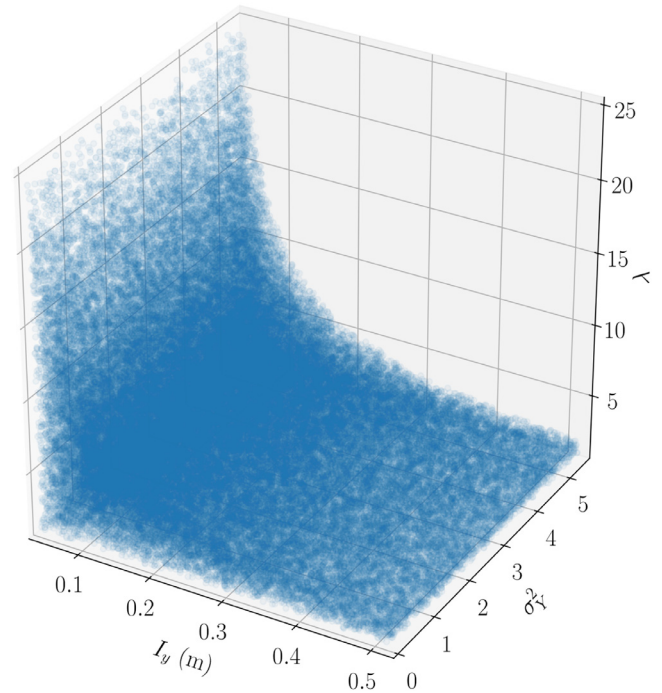

Fig. 1. Generated sample of size $P = 10^5$ of geostatistical parameters $\mathbf{m} = (\sigma_Y^2, I_y, \lambda)$ drawn from a joint pdf $\pi(\mathbf{m})$. Each realization is used together with an associated $\mathbf{R}$-realization to create a log-hydraulic conductivity field on which flow and transport simulations are performed.

2.4.1. Generation of hydraulic conductivity fields

The log-hydraulic conductivity field realizations $Y(\mathbf{x})$ are generated using the fast circulant embedding technique (see Dietrich and Newsam, 1997 for details). A given realization depends on the specified geostatistical model parameters and $\mathbf{R}$; a 250×250 a random draw from a standard normal distribution. The geostatistical model parameters determine the spatial regularity (smoothness class), while $\mathbf{R}$ determines the locations of high and low log-hydraulic conductivity values relative to the mean value μ_Y of the geostatistical model. Here μ_Y is fixed at -6 while remaining parameters are treated as random variables $\mathbf{m} = (\sigma_Y^2, I_y, \lambda)$ described by a joint probability density function (PDF) $\pi(\mathbf{m})$. The variance σ_Y^2 is randomly drawn from a uniform PDF with support $[0, 5.5]$, the integral scale I_y is drawn from a log-uniform PDF with support $[L/25, L/2]$ m, and the anisotropy factor λ ($= I_x/I_y$) is drawn from a uniform PDF with support $[1, L/I_y]$ (i.e., conditionally on I_y). The discretization implies that heterogeneities obtained with the smallest integral scales are resolved with at least 10 cells in each direction. The log-uniform distribution of I_y is here chosen to favor realizations with finely structured fields. The generated sample of the geostatistical model parameters of size $P = 10^5$ is represented in Fig. 1. Note that each draw is associated with a unique $\mathbf{R}$, which together form a log-hydraulic conductivity field realization.

2.4.2. Flow simulations

The groundwater flow equation (Eq. (3)) is solved numerically using the open-source finite-difference solver MODFLOW-2005 (Harbaugh, 2005). The prescribed boundary conditions are a horizontal head gradient of 0.05 inducing flow from left to right and no-flow conditions for the top and bottom boundaries. The head gradient value was chosen such that for a homogeneous field equal to $exp(\mu_Y)$ the tracer arrival time occurs approximately at half of the simulated time-duration of the tracer experiment. In the simulations, the hydraulic conductivity between two adjacent cells is taken as their harmonic mean. The chosen

numerical scheme used to solve the system of linear equations is the preconditioned conjugate gradient method (Hill, 1990).

2.4.3. Transport simulations

The advection-diffusion equation (Eq. (5)) is solved using the groundwater solute transport simulator package MT3D-USGS (Bedekar et al., 2016). The initial condition is a homogeneous concentration field of 0.01 g l^{-1} and the boundary conditions are: (i) constant concentration of 1 g l^{-1} along the left boundary (ii) no-flux along the top and bottom boundaries and (iii) free-flux along the right boundary. The porosity is assumed constant and equal to 0.3. For the advection term in Eq. (5), the third-order Total Variation Diminishing (TVD) approach (Cox and Nishikawa, 1991) is used. The TVD solver was found to be very robust and showed minimal numerical dispersion when benchmarked against planar fronts. Nevertheless, in order to mask the small numerical dispersion, the diffusion coefficient was slightly increased from $D_m = 1.6 \times 10^{-9}$ m^2 s^{-1} (the standard value for the diffusion coefficient of salt in water) to $D_m = 2 \times 10^{-8}$ m^2 s^{-1}. The latter (larger) value is obtained by fitting the analytical solution for a concentration profile for a step injection in 1-D (e.g., Ogata and Banks, 1961) to a TVD-calculated concentration profile obtained for a homogeneous hydraulic conductivity field equal to μ_Y when the diffusion coefficient is imposed to be the one of salt in water. Each simulated tracer experiment lasts for 4×10^3 s and during this time period, 400 equidistant samples $c_i(\mathbf{x})$ ($i = 1, \ldots, 400$) of the simulated concentration fields are recorded at times $t = (i-1)\Delta t$, with $\Delta t = 4 \times 10^3$ s/400 = 10 s. The injected tracer typically does not fully replace the initial background tracer at the end of the simulation period. This is a consequence of the short simulation time imposed by computational constraints and large low-velocity regions. The mean Péclet number is $\sim 6 \times 10^3$, defined as $Pe = \frac{\bar{u}}{D_m}$, where $\bar{u}$ is the tracer velocity for the constant hydraulic conductivity field.

2.4.4. Electrical simulations

For each sampled concentration field $c_i(\mathbf{x})$, the 2-D square domain is alternatively excited by imposing an electrical potential difference of 1 V with a pair of line electrodes along either the vertical or horizontal boundaries of the sample. The remaining boundaries are prescribed zero electrical potential gradient normal to the boundaries. The resulting electrical potential fields $\phi_i^H(\mathbf{x})$ and $\phi_i^V(\mathbf{x})$ associated to the horizontal and vertical modes, respectively, are computed by numerically solving the Laplace equation (Eq. (8)) with the finite-element solver module of the Python library pyGIMLi (Rücker et al., 2017). For simplicity, the input electrical conductivity distribution $\sigma_i(\mathbf{x})$, used for solving the boundary-value problems at each time step is assumed to be perfectly and linearly related to the transport simulation output $c_i(\mathbf{x})$. The resulting normalized dimensionless time-series denoted as σ^H, σ^V and M vary within [0.01, 1]. The data generation is summarized by the pseudo-code in Algorithm 1.

3. Inference problem

We are interested in assessing to what extent the time-series σ^H, σ^V and M may constrain the geostatistical parameters $\mathbf{m} = (\sigma_Y^2, I_y, \lambda)$. We consider the following five combinations of time-series:

$$\mathbf{d}_H := \{\sigma^H\},$$

$$\mathbf{d}_V := \{\sigma^V\},$$

$$\mathbf{d}_M := \{M\},$$

$$\mathbf{d}_{HV} := \{\sigma^H, \sigma^V\},$$

$$\mathbf{d}_{HVM} := \{\sigma^H, \sigma^V, M\}.$$

The data vectors $\mathbf{d}_H, \mathbf{d}_V$ and $\mathbf{d}_M$ are used to assess the individual performance of each type of time-series; $\mathbf{d}_{HV}$ is used to evaluate the

---

Algorithm 1: Data generation procedure.

```
for j = 1 to 10^5 do
    Draw geostatistical model realization m = (σ_Y^2, I_y, λ)
    and R
    Generate hydraulic conductivity field K(x)
    Simulate steady-state Eulerian flow field q(x)
    for i = 1 to 400 do
        Specify sampling time t as t = (i - 1)Δt
        Simulate concentration field c_i(x)
        Compute M_i, σ_i^H and σ_i^V
    end

    Save K(x)
    Save concentration field time-series
    C = [c_1(x), ..., c_400(x)]
    Save time-series of mass breakthrough
    M = [M_1, ..., M_400]  and electrical conductivity
    σ^H = [σ_1^H, ..., σ_400^H]  and σ^V = [σ_1^V, ..., σ_400^V]
end
```

---

performance of electrical data alone and $\mathbf{d}_{HVM}$ is used to evaluate the value of using all the data at the same time. We cast the problem as a Bayesian inference framework as outlined below.

3.1. Bayesian inference framework

In a finite-dimensional Bayesian inference framework, a model is described in terms of M random variables with realizations $\mathbf{m} = (m_1, \ldots, m_M)$ that can be used as input to a physical forward simulator producing N simulated data $\mathbf{d}^{sim} = \mathcal{F}(\mathbf{m})$ (e.g., Gelman et al., 2013; Tarantola, 2005). The prior probability density function $\pi(\mathbf{m})$ is updated using Bayes' theorem to a posterior probability density function $\pi(\mathbf{m}|\mathbf{d}^{obs})$ after considering the observed data $\mathbf{d}^{obs} = (d_1, \ldots, d_N)$ using a likelihood function $\pi(\mathbf{d}^{obs}|\mathbf{m})$. This function evaluates the likelihood of any model realization given and the residual error vector $\mathbf{e} = \mathbf{d}^{obs} - \mathbf{d}^{sim}$ and an assumed underlying observational noise model (e.g., Tarantola, 2005). Bayes' theorem in its unnormalized form reads:

$$\pi(\mathbf{m}|\mathbf{d}^{obs}) \propto \pi(\mathbf{d}^{obs}|\mathbf{m})\pi(\mathbf{m}). \tag{11}$$

In our context, the prior is given by the PDF described in Section 2.4.1 and $\mathbf{d}^{obs}$ is the noise-contaminated output of the forward simulator, $\mathcal{F}(\mathbf{m}_t)$, when evaluated using one of the test cases $\mathbf{m}_t$ described in Section 4.2. For the electrical time-series, $\mathcal{F}(\mathbf{m})$ is formed by the sequential application of the following forward mappings: (i) the realization of the hydraulic conductivity field $K(\mathbf{x})$, (ii) solving the groundwater flow Eq. (3), (iii) the advection-diffusion Eq. (5), (iv) the Laplace Eq. (8) and (v) evaluating the equations defining σ^H (9) and σ^V (10).

3.2. Posterior density approximation

In Bayesian inference, Monte Carlo (MC) sampling can be used to approximate $\pi(\mathbf{m}|\mathbf{d}^{obs})$ by a MC integration over a finite sample of the sought distribution (e.g., Mosegaard and Tarantola, 1995; Gelman et al., 2013). The simplest approach is Acceptance-Rejection Sampling (ARS), which consists of drawing samples $\mathbf{m}$ proportionally to the prior density and accepting them as samples of the posterior density proportionally to their likelihood $\pi(\mathbf{d}^{obs}|\mathbf{m})$. This is an exact sampling method (e.g., Mosegaard and Tarantola, 1995) and it can be used off-line using a large ensemble of prior model realizations given that, unlike in a Markov Chain MC (MCMC) sampling method, there is no dependence between the model proposals. Its main disadvantage is that, since the parameter search is unguided (unlike MCMC), the probability of acceptance

decreases exponentially with the dimensionality M of the model parameter space. As more dimensions are added to the problem, the ratio of the (hyper)volume of high likelihood values (regions of large acceptance probability), to the total volume of the model space, decreases exponentially to zero (e.g., Scales, 1996; Curtis and Lomax, 2001). This so-called curse of dimensionality may result in unrealistically-large prior model samples, even when addressing only a handful of parameters. In the context of this study, we are interested in only three geostatistical parameters (Section 2.1) possibly suggesting that ARS could be a good choice.

However, when the scale of the modelling domain is insufficiently large compared to the integral scales of the field $Y(\mathbf{x})$ under consideration, ergodic conditions are not fulfilled implying a potentially high dependence on $\mathbf{R}$ (Section 2.4.1). This high-dimensional variable is different for each realization of $Y(\mathbf{x})$ and it ultimately controls the locations of high- and low hydraulic conductivity regions. Even if we are uninterested in $\mathbf{R}$ as such, it forms part of our data generation process and, thus, it enters the inference problem as a nuisance variable (e.g., Gelman et al., 2013) that needs to be accounted for. Consequently, our definition of the forward simulator given above has to be expanded to $\mathcal{F}(\mathbf{m}, \mathbf{R})$. Assuming independence of $\mathbf{m}$ and $\mathbf{R}$ examples, the actual inference problem to solve reads

$$\pi(\mathbf{m}, \mathbf{R}|\mathbf{d}^{obs}) \propto \pi(\mathbf{d}^{obs}|\mathbf{m}, \mathbf{R})\pi(\mathbf{m})\pi(\mathbf{R}). \tag{12}$$

To obtain the sought density, we need to marginalize $\pi(\mathbf{m}, \mathbf{R}|\mathbf{d})$ with respect to $\mathbf{R}$:

$$\pi(\mathbf{m}|\mathbf{d}) = \int \pi(\mathbf{m}, \mathbf{R}|\mathbf{d})d\mathbf{R}. \tag{13}$$

Due to its higher dimensionality (more than 62,500 variables in our examples), the problem expressed by Eq. (12) is practically impossible to handle with the formal Bayesian ARS algorithm. For this reason, we resort to an approximate version of the ARS that is outlined in the following subsection.

3.2.1. ABC acceptance-rejection sampling algorithm

The ARS algorithm implemented within an Approximate Bayesian Computational (ABC) framework, labelled Approximate Acceptance-Rejection Sampling (AARS) algorithm from now on, is an approximate sampling method that produces a smooth approximation of $\pi(\mathbf{m}|\mathbf{d})$. The reader is referred to (Sisson et al., 2018) for an overview on ABC methods. The AARS algorithm requires two additional inputs: (i) a distance metric $\rho(\mathbf{d}^{sim}, \mathbf{d}^{obs})$ for comparing the calculated data with the observed data and (ii) a kernel density function $\mathbf{K}_h(\rho)$ for weighting the distance metric and defining an acceptance probability. Together, they replace the likelihood function.

In our work, the distance metric $\rho(\mathbf{d}^{sim}, \mathbf{d}^{obs})$ is taken as the L_1-norm:

$$\rho(\mathbf{d}^{sim}, \mathbf{d}^{obs}) = \frac{1}{N} \sum_{1}^{N} |\mathbf{d}^{sim} - \mathbf{d}^{obs}| \tag{14}$$

and the Kernel density is chosen to be a uniform function:

$$\mathbf{K}_h(\rho) = \begin{cases} 1 & 0 \leq \rho/h \leq 1 \\ 0 & 1 < \rho/h, \end{cases} \tag{15}$$

where the acceptance bandwidth h is chosen such that the 0.5th percentile of the distribution of ρ ordered from the lowest to the highest distance are accepted. In our case, this means that $\mathbf{K}_h(\rho)$ accepts the models producing the $S = 500$ lowest distances out of the $K = 10^5$ sampled prior samples.

The AARS algorithm, described in pseudo-code in Algorithm 2, proceeds similarly to the formal ARS algorithm.

Considering Algorithm 2, it can be noticed that the AARS algorithm draws samples from the joint distribution

$$\pi^{AARS}(\mathbf{m}, \mathbf{R}, \mathbf{d}|\mathbf{d}^{obs}) = \mathbf{K}_h(\rho)\pi(\mathbf{d}^{obs}|\mathbf{d}, \mathbf{m}, \mathbf{R})\pi(\mathbf{m})\pi(\mathbf{R}), \tag{16}$$

Algorithm 2: Approximate Acceptance-Rejection Sampling (AARS) algorithm.

for $k = 1, \ldots, P$ **do**

    Draw $\mathbf{m}_{(k)}$ from $\pi(\mathbf{m})$ and $\mathbf{R}_{(k)}$ from $\pi(\mathbf{R})$

    Generate a data instance $\mathbf{d} = \mathbf{d}^{sim}$ from the underlying unobserved likelihood $\pi(\mathbf{d}^{obs}|\mathbf{d}, \mathbf{m}_{(k)}, \mathbf{R}_{(k)})$

    Accept $\mathbf{m}_{(k)}$ with an acceptance probability $AP = \mathbf{K}_h(\rho)$

end

---

which, when integrated over all generated data instances gives the AARS approximation of the ($\mathbf{R}$-marginalized) posterior density:

$$\pi^{AARS}(\mathbf{m}|\mathbf{d}^{obs}) = \int \pi^{AARS}(\mathbf{m}, \mathbf{R}, \mathbf{d}|\mathbf{d}^{obs})d\mathbf{d}; \tag{17}$$

or,

$$\pi^{AARS}(\mathbf{m}|\mathbf{d}^{obs}) = \pi(\mathbf{m}) \int \mathbf{K}_h(\rho)\pi(\mathbf{d}^{obs}|\mathbf{d}, \mathbf{m}, \mathbf{R})d\mathbf{d}. \tag{18}$$

As pointed out by Sisson et al. (2018), from Eq. (18) the AARS can be interpreted as a formal Bayesian ARS algorithm using an approximated likelihood function that is a Kernel Density Estimation (KDE) of the true likelihood:

$$\pi^{AARS}(\mathbf{d}^{obs}|\mathbf{m}, \mathbf{R}) = \int \mathbf{K}_h(\rho)\pi(\mathbf{d}^{obs}|\mathbf{d}, \mathbf{m}, \mathbf{R})d\mathbf{d}. \tag{19}$$

For building the empirical posterior probability densities, we perform KDE over the samples obtained from $\pi^{AARS}(\mathbf{m}|\mathbf{d}^{obs})$. For consistency, the prior PDF (Section 2.4.1) is computed by performing KDE over the generated sample of size $P = 10^5$. The KDE approach is described in the following subsection.

3.2.2. Multivariate kernel density estimation (KDE)

Given a sample $\mathbf{X} = \{\mathbf{x}_1, \ldots, \mathbf{x}_S\}$ of size S of M-variate random vectors belonging to a common distribution described by the density g, the KDE estimator $\hat{g}$ of g is given by (e.g., Wand and Jones, 1994)

$$\hat{g}_{\mathbf{H}}(\mathbf{x}) = \frac{1}{S} \sum_{i=1}^{S} \mathbf{K}_{\mathbf{H}}(\mathbf{x} - \mathbf{x}_i), \tag{20}$$

with the estimator function $\mathbf{K}_{\mathbf{H}}$ defined as:

$$\mathbf{K}_{\mathbf{H}}(\mathbf{x}) = |\mathbf{H}|^{-\frac{1}{2}} K(\mathbf{H}^{-\frac{1}{2}}\mathbf{x}), \tag{21}$$

where the kernel function K is a symmetric multivariate density. Furthermore, $|\mathbf{H}|$ is the determinant of the $M \times M$ bandwidth matrix $\mathbf{H}$, which is symmetric and positive definite in general and, if the M variables are assumed independent, it is diagonal with entries $\mathbf{H}_i$ given as $\sqrt{\mathbf{H}_i} = h\sigma_i$, where h is the bandwidth parameter and σ_i the standard deviation of the ith component of the random variable.

The estimator of Eq. (20) is an average of kernel densities that are centered at the sample points and whose decay is controlled by $\mathbf{H}$. The particular choice of K does not substantially influence the performance of the KDE approach, but the choice of the bandwidth h, defining $\mathbf{H}$ (i.e., the tails of K), is a most crucial aspect, given that under- or over-smoothed estimators will be produced if it is taken too small or large, respectively (e.g., Wand and Jones, 1994). In the present work, K is chosen as the standard multivariate normal function

$$\mathbf{K}_{\mathbf{H}}(\mathbf{x}) = (2\pi)^{-\frac{N}{2}} |\mathbf{H}|^{-\frac{1}{2}} exp\left\{ -\frac{1}{2}\mathbf{x}^{\mathbf{T}}\mathbf{H}^{-1}\mathbf{x} \right\}. \tag{22}$$

For h, a common choice when dealing with unimodal distributions, as the ones expected in this study, is based on Silverman's rule of thumb (e.g., Silverman, 1986):

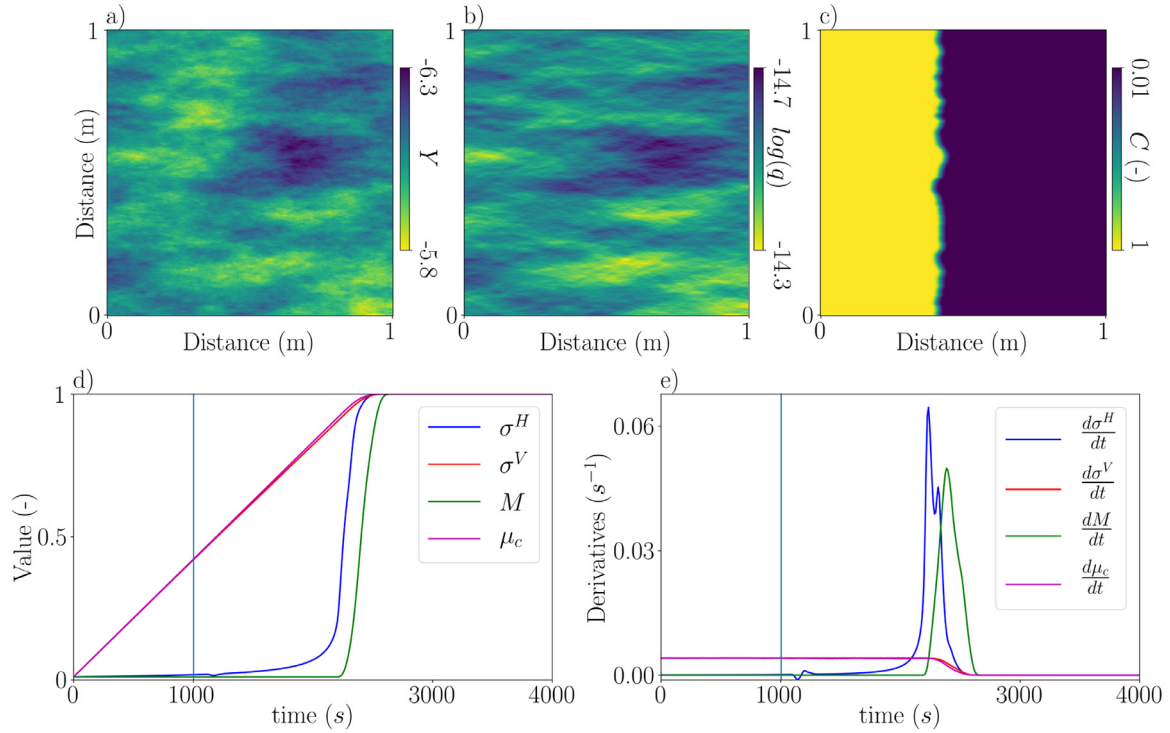$$h_s = \frac{4}{M + 2}^{\frac{1}{M+4}} d^{-\frac{1}{M+4}}. \tag{23}$$

Fig. 2. (Color online) (a) Weakly heterogeneous hydraulic conductivity field with geostatistical parameters $(\sigma_Y^2, I_y, \lambda) = (0.005, 0.130\,\text{m}, 3.179)$. (b) Corresponding steady-state flow field and (c) normalized concentration field at time 10^3 s. (d) Time-series of the horizontal and vertical equivalent electrical conductivity, mass-flux, and mean tracer concentration, denoted σ^H, σ^V, M and μ_c, respectively. The light-blue vertical line, also present in (e), marks the time 10^3 s of the concentration field shown in (c). (e) Time-derivatives of σ^H, σ^V, M and μ_c.

The reliability of the used information measure (Subsection 3.3) largely depends on the quality of the input density estimations provided by the KDE approach (e.g., Budka et al., 2011). Considering the trade-offs pertaining to the choice of h, a manual tuning process was necessary, which resulted in the choice of $h = 0.75 h_s$ for the results presented herein.

3.3. Information measure: Kullback–Leibler divergence

The degree of knowledge brought by the observed data $\mathbf{d}^{obs}$ pertaining to the geostatistical model parameters is evaluated by comparing our approximation of $\pi(\mathbf{m}|\mathbf{d}^{obs})$ with $\pi(\mathbf{m})$. The Kullback–Leibler divergence (KLD) (Kullback and Leibler, 1951), also termed Relative Information Content (Tarantola, 2005), is probably the most widely used quantitative measure for comparing PDFs:

$$KLD(\pi(\mathbf{m}|\mathbf{d}^{obs}); \pi(\mathbf{m})) = \int \pi(\mathbf{m}|\mathbf{d}^{obs}) ln\left(\frac{\pi(\mathbf{m}|\mathbf{d}^{obs})}{\pi(\mathbf{m})}\right) d\mathbf{m}, \qquad (24)$$

where the base of the logarithm is taken as e, giving the information in units of nats (e.g., Cover and Thomas, 2012). The integration of Eq. (10) is performed over the support of the densities and the KLD is finite as the support of $\pi(\mathbf{m}|\mathbf{d}^{obs})$ is contained in the support of $\pi(\mathbf{m})$ (e.g., Cover and Thomas, 2012). The KLD is zero when $\pi(\mathbf{m}|\mathbf{d}^{obs}) \equiv \pi(\mathbf{m})$ (i.e., the data carry no information about the model parameters) and it increases as the posterior becomes more compact with respect to the prior as a consequence of conditioning to the data. Note that when the prior and posterior densities are Gaussian with the same mean, but the standard deviation of the posterior is half the standard deviation of the prior, then the KLD is 0.27 nats.

Since our samples are drawn from approximate posterior densities $\pi^{AARS}(\mathbf{m}|\mathbf{d}^{obs})$ that are KDE (i.e., smoothed) versions of the target densities $\pi(\mathbf{m}|\mathbf{d}^{obs})$ (Eq. (18)), the chosen AARS approach provides a conservative framework for assessing the information content in terms of

the KLD measure, since it is always true that

$$KLD(\pi^{AARS}(\mathbf{m}|\mathbf{d}^{obs}); \pi(\mathbf{m})) < KLD(\pi(\mathbf{m}|\mathbf{d}^{obs}); \pi(\mathbf{m})), \qquad (25)$$

which implies that the information content in the considered time-series is at least as large as the estimates obtained by our analysis.

4. Results

We first show two examples of generated data for end-member cases of weak and strong hydraulic heterogeneity. Then, we describe the results obtained for different geostatistical parameter value combinations in terms of the KLD and bias measures. In doing so, we discuss results obtained for one $\mathbf{R}$-realization, as well as ensemble statistics deduced from 50 $\mathbf{R}$-realizations.

4.1. Two examples of generated data

Fig. 2 shows an example of data obtained for a weakly heterogeneous hydraulic conductivity field with $(\sigma_Y^2, I_y, \lambda) = (0.005, 0.130\,\text{m}, 3.179)$ (Fig. 2a), resulting in an approximately constant flow field (Fig. 2b). The corresponding concentration field, shown at the sampling time 10^3 s, when the tracer occupies approximately 50% of the model domain, displays an overall planar front (Fig. 2c).

The time-series of σ^H and σ^V (Fig. 2d) evolve according to the lower and upper Wiener bounds. These upscaling formulas for laminated materials (e.g., Milton and Sawicki, 2003) correspond to the harmonic and arithmetic means of the local electrical conductivities, respectively. The arithmetic averaging governing σ^V is manifested by linear scaling with time. In this case, σ^V forms an almost perfect predictor of the mean salinity (μ_c) within the sample. σ^H, on the contrary, strongly underestimates μ_c. For this case, the mean velocity of the tracer front is given by the time-derivative of σ^V (Fig. 2e), information that is available before the mass-flux (M) time-series shows any response.
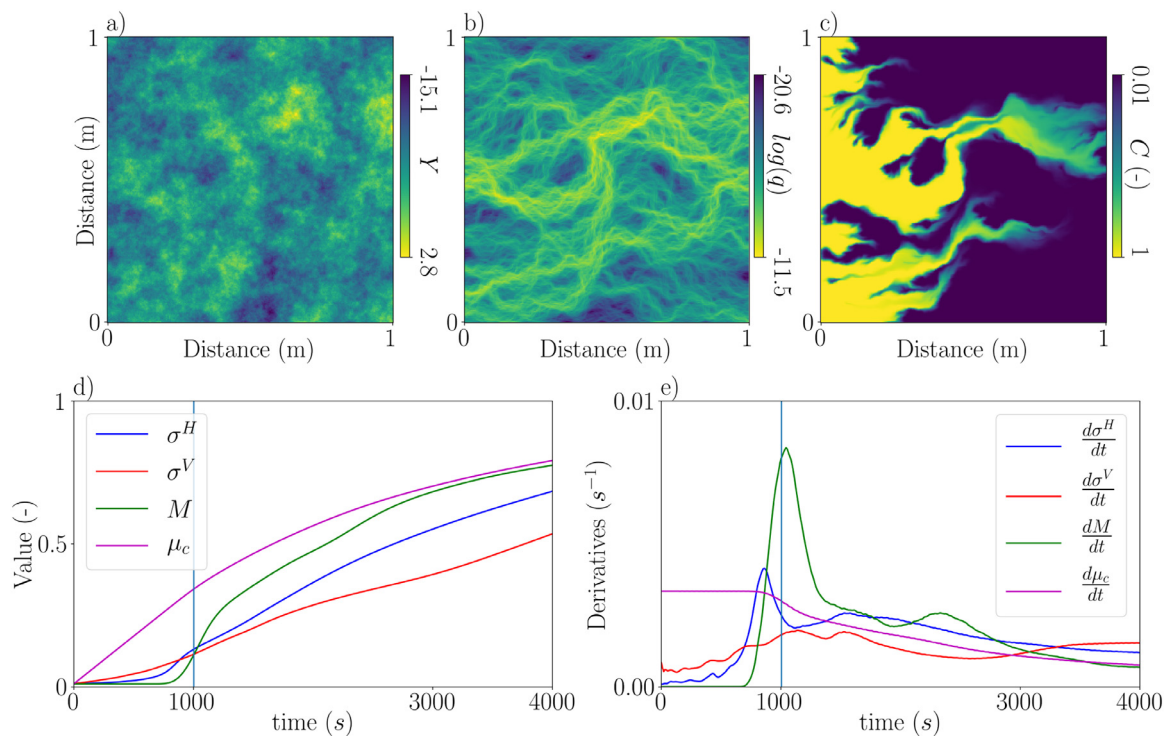
Fig. 3. (Color online) (a) Strongly heterogeneous hydraulic conductivity field, defined with geostatistical parameters $(\sigma_Y^2, I_y, \lambda) = (5.111, 0.085\,\text{m}, 1.028)$. (b) Corresponding steady-state flow field and (c) normalized concentration field at time 10^3 s. (d) Time-series of the horizontal and vertical equivalent electrical conductivity, mass-flux, and mean tracer concentration, denoted σ^H, σ^V, M and μ_c, respectively. The light-blue vertical line, also present in (e), marks the time 10^3 s, of the concentration field in (c). (e) Time-derivatives of σ^H, σ^V, M and μ_c. The large peaks exhibited by $\frac{d\sigma^H}{dt}$ and $\frac{dM}{dt}$ approximately coincide with the first arrival of the tracer at the outlet.

These easily interpretable results are now contrasted with those obtained for a strongly heterogeneous hydraulic conductivity field, defined with $(\sigma_Y^2, I_y, \lambda) = (5.111, 0.085\,\text{m}, 1.028)$. The resulting field has small-scale structures and is close to isotropic (Fig. 3a). Yet its associated flow field exhibits pronounced channeling (Fig. 3b) resulting in a highly heterogeneous concentration field (Fig. 3c). Neither σ^H nor σ^V follow any known upscaling law. They both start to vary much earlier than M (Fig. 2d), which only reacts when the tracer arrives at the outlet. These early variations are clearly seen in the time-derivatives of the electrical responses (Fig. 2e), which are non-zero from the moment the tracer injection starts and exhibit small peaks that are related to internal connection events of the solute that are invisible to M. Both σ^H and M show a steep increase around 10^3 s, and a large peak in their time-derivatives, corresponding to early breakthrough arrival. For this case, μ_c is at early times much larger than all data and is asymptotically approximated by M, followed in order of magnitude by σ^H and σ^V.

4.2. Test cases

We now apply the Bayesian inference approach using three different combinations of the geostatistical model parameter values:

- (i) $\mathbf{m}_1 := (4.70, 0.06\,\text{m}, 1.50)$. This leads to a strongly heterogeneous hydraulic conductivity field that is approximately isotropic and exhibits small structures (Fig. 4a).
- (ii) $\mathbf{m}_2 := (0.80, 0.06\,\text{m}, 10.00)$. This leads to a mildly-to-moderately heterogeneous field that exhibits a high degree of layering (Fig. 4d).
- (iii) $\mathbf{m}_3 := (4.70, 0.38\,\text{m}, 1.50)$. This leads to a highly heterogeneous field exhibiting large-scale structures (Fig. 4g).

In Fig. 4, example realizations of generated log-hydraulic conductivity fields for the three test cases are shown together with their corresponding flow and concentration fields.

4.3. Information assessment of data types

For each test case of the model vector $\mathbf{m}$, 50 datasets $\mathbf{d}_j^{obs}$ (Section 3) are simulated using hydraulic conductivity fields created with different $\mathbf{R}$-realizations. The forward responses are contaminated with noise having zero mean and a mean deviation of 0.005 representing 50% of the baseline electrical conductivity. The evaluation of the different data types and geostatistical parameter values is considered both in terms of the ensemble of realizations (ensemble performance) and in terms of randomly-picked single realizations (i.e., the fields shown in Fig. 4). In addition to the estimated joint posterior PDF, we also consider the corresponding marginal distributions to evaluate the ability of the data to constrain individual geostatistical parameters. For the marginal analysis, we also consider a relative bias measure, computed as the ratio of the mean bias of the marginal posteriors, with respect to the true values of $\mathbf{m}$, to the mean bias of the marginal priors with respect to the true values. From now on, we drop the superscript "*obs*" when referring to the observed conditioning data.

4.3.1. Test case $\mathbf{m}_1$

Table 1 summarizes the results obtained for test case $\mathbf{m}_1$.

When considering the joint KLDs obtained for the ensemble of realizations, we find that $\mathbf{d}_{HV}$ has the largest mean KLD, closely followed by $\mathbf{d}_{HVM}$. The least informative data type $\mathbf{d}_M$ has a mean KLD that is $\sim 75\%$ of the one for $\mathbf{d}_{HV}$, while $\mathbf{d}_H$ and $\mathbf{d}_V$ have values in-between. The KLD standard deviations have similar values among all the data types and represent $\sim 20\%$ of the mean values.

We now turn to the results obtained for the fields in Fig. 4a–c and the corresponding time-series highlighted in Fig. 5a–c. For this specific realization, the KLDs span a small range of only $\sim 13\%$. Also, the ordering is different and the most and least informative data sets for this case are $\mathbf{d}_H$ and $\mathbf{d}_V$, respectively. This illustrates (together with the standard de-
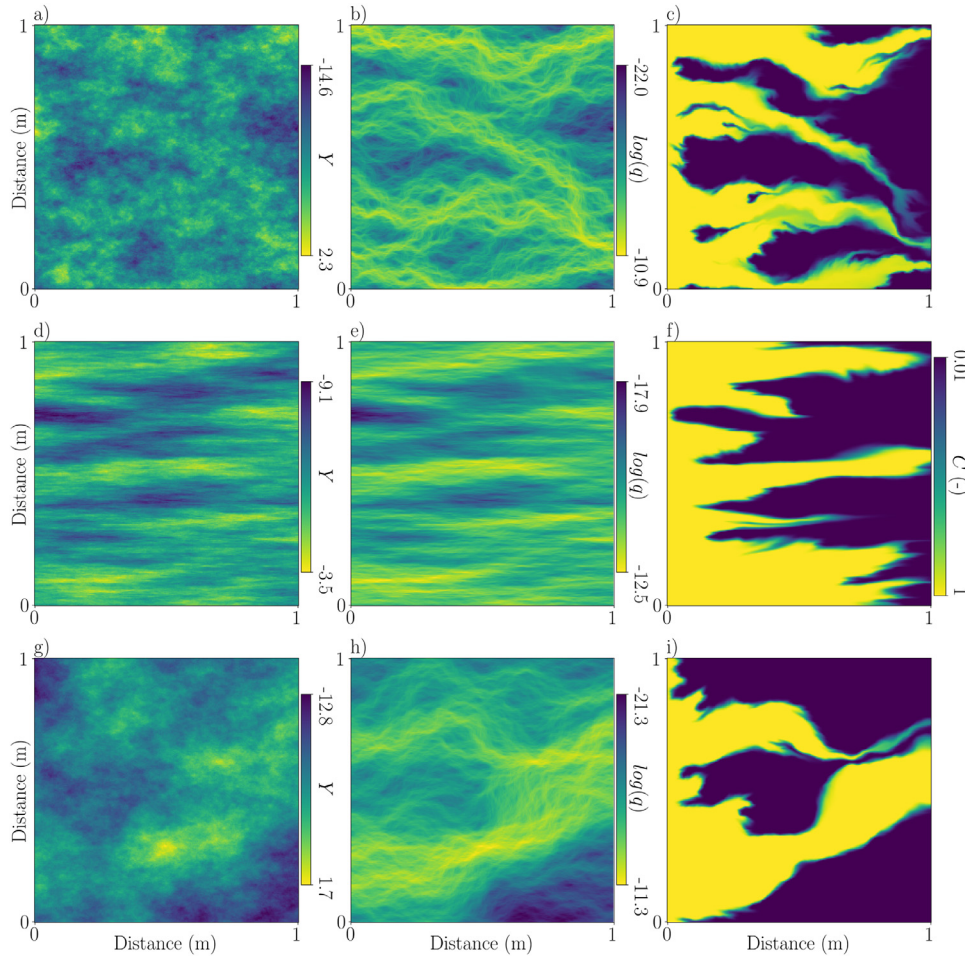
Fig. 4. (a, d, f) Realizations of log-hydraulic conductivity fields and (b, e, h) associated flow and (c, f, i) concentration fields at time 10^3 s for the three evaluated test cases (a–c) $\mathbf{m}_1$, (d–f) $\mathbf{m}_2$ and (g–i) $\mathbf{m}_3$. Note that the locations of high- and low hydraulic conductivity regions are governed by random $\mathbf{R}$-realizations.

Table 1

KLDs and mean relative biases of $\mathbf{m}_1$ for the different conditioning data types. Columns 1 and 2 show the mean μ_{KLD} and standard deviation σ_{KLD} of the KLDs using the ensemble of hydraulic conductivity realizations. Column 3 shows the KLD values for the joint posterior PDFs using one realization of the conditioning data obtained from Fig. 4a–c and highlighted in Fig. 5a–c. The subsequent pairs of columns show the marginal KLD values and relative mean biases for the marginal posteriors of each component of $\mathbf{m}_1$ using this specific realization.

	Ensemble		$\mathbf{m}$	σ_Y^2		I_y (m)		λ	
	μ_{KLD}	σ_{KLD}	KLD	KLD	Bias	KLD	Bias	KLD	Bias
$\mathbf{d}_H$	0.8171	0.1445	0.7351	0.3754	0.5018	0.1418	0.7560	0.0904	0.8525
$\mathbf{d}_V$	0.8016	0.1131	0.6418	0.2617	0.6703	0.1021	0.6760	0.0675	1.2163
$\mathbf{d}_M$	0.6625	0.1580	0.6973	0.2153	0.8223	0.1771	0.5325	0.0980	1.1271
$\mathbf{d}_{HV}$	0.8830	0.1352	0.6937	0.2501	0.6716	0.1536	0.7058	0.0899	0.7971
$\mathbf{d}_{HVM}$	0.8712	0.1318	0.6985	0.2386	0.7232	0.1537	0.7189	0.1050	0.7672

viations of the KLDs discussed above) the stochastic variations that are inherent under non-ergodic conditions. The variability in the generated data due to variations in the $\mathbf{R}$-realizations, for a given geostatistical model, is indicated by the insets in Fig. 5a–c.

The posterior model samples obtained by the AARS algorithm and used for building the empirical posterior PDFs for each type of data are shown in Fig. 5. The density distribution of these 3-D clouds of points convey a qualitative view of the ability of the different data types to constrain the geostatistical parameters. No eye-catching differences distinguish the different point clouds, reflecting the rather similar values of the associated KLDs.

The KLDs computed for the marginal posterior PDFs, labelled marginal KLDs from now on, are the largest for σ_Y^2, followed by I_y and λ,

that on average, represent $\sim$ 50% and $\sim$ 25% of the KLDs of σ_Y^2, respectively. We find that σ_Y^2 is best constrained by $\mathbf{d}_H$, producing the largest marginal KLD and the smallest bias. For this parameter, the poorest performance is achieved by $\mathbf{d}_M$ that has both the smallest marginal KLD and the largest bias. This can be seen in the estimated marginal posterior probability density (Fig. 6a) displaying a mass distribution which is the furthest away from the true value $\sigma_Y^2 = 4.70$. For I_y, on the contrary, $\mathbf{d}_M$ features the highest marginal KLD and the smallest bias (Fig. 6b). The ability of the data to constrain λ is low (Fig. 6c) with $\mathbf{d}_{HVM}$ featuring the highest marginal KLD. The relative mean biases are negatively correlated with the associated KLD measure, showing consistency between the two measures.
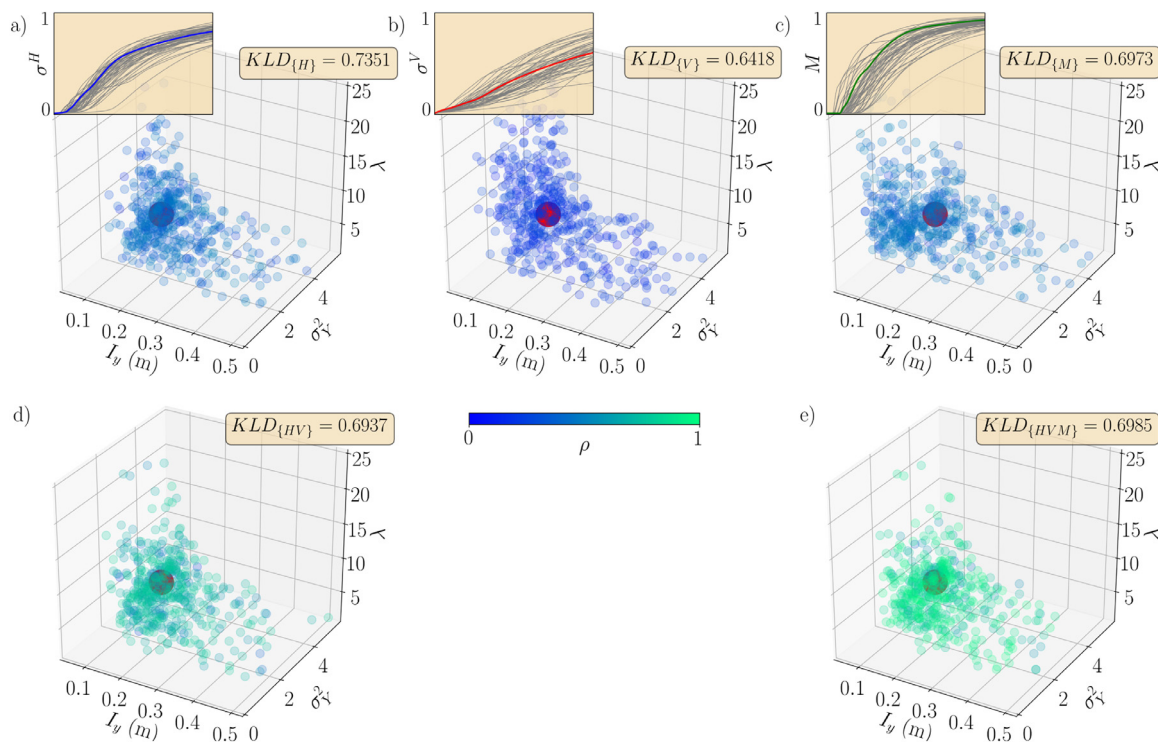
Fig. 5. Posterior model parameter vector samples of size $S = 500$ obtained by the AARS algorithm for test case $\mathbf{m}_1 = (4.7, 0.06\,\mathrm{m}, 1.5)$ using different datasets as conditioning data. The colored clouds of points represent the samples for datasets (a) $\mathbf{d}_H$; (b) $\mathbf{d}_V$; (c) $\mathbf{d}_M$; (d) $\mathbf{d}_{HV}$; (e) $\mathbf{d}_{VM}$; (f) $\mathbf{d}_{HVM}$. The colormap encodes the L_1 distance ρ between simulated and observed data, normalized by the minimum and maximum values of ρ of the test case. The inset plots of (a), (b) and (c) show, respectively, the 50 realizations of time-series σ^H, σ^V and M generated for $\mathbf{m}_1$ using different $\mathbf{R}$-realizations. The data considered here for inference are shown by thick-colored curves. The resulting KLD values are given for each dataset.
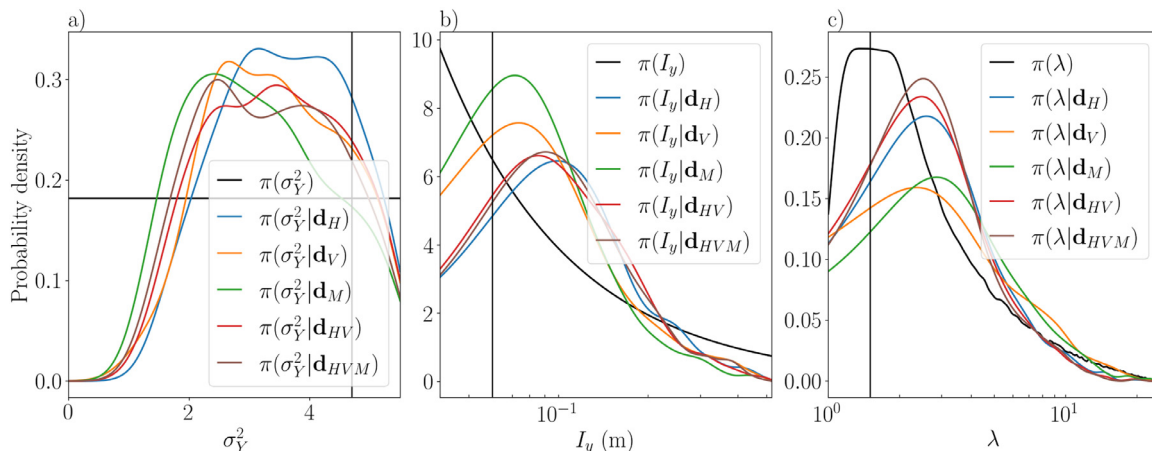

Fig. 6. (Color online) Marginal posterior PDFs associated to each type of conditioning data $\mathbf{d}_H$, $\mathbf{d}_V$, $\mathbf{d}_M$, $\mathbf{d}_{HV}$, $\mathbf{d}_{VM}$ and $\mathbf{d}_{HVM}$ for test case $\mathbf{m}_1 = (4.7, 0.06\,\mathrm{m}, 1.5)$. Marginal prior and posterior PDFs corresponding to (a) σ_Y^2 (b) I_y and (c) λ.

4.3.2. Test case m₂

Table 2 summarizes the results obtained for test case $\mathbf{m}_2$.

When considering the joint posterior KLDs for the ensemble, we find that $\mathbf{d}_{HVM}$ is the most informative dataset followed by $\mathbf{d}_H$ and $\mathbf{d}_{HV}$. Far behind, featuring mean KLDs that are $\sim 60\%$ of $\mathbf{d}_{HVM}$, are $\mathbf{d}_V$ and $\mathbf{d}_M$. Of the individual data sets, we find that $\mathbf{d}_H$ is much more informative than $\mathbf{d}_V$ and $\mathbf{d}_M$. The standard deviations have similar magnitudes and represent $\sim 20 - 35\%$ of the mean values.

We now consider the results obtained using the time-series (Fig. 7a–c) obtained from the fields in Fig. 4d–f. The ranking for the joint KLDs are similar to the ensemble mean KLDs, except that $\mathbf{d}_H$ performs the

best. The point clouds of the posterior samples (Fig. 7) clearly shows that $\mathbf{d}_H$ (Fig. 7a) constrain the geostatistical model parameters much better than $\mathbf{d}_V$ (Fig. 7b) and $\mathbf{d}_M$ (Fig. 7c).

The marginal KLDs are again the largest for σ_Y^2, followed by those of I_y and λ. We find that σ_Y^2 is the most constrained by $\mathbf{d}_H$ and the least constrained by $\mathbf{d}_M$ as reflected by their marginal KLDs and the compactness of their posterior PDFs (Fig. 8a). All the marginal PDFs for σ_Y^2 exhibit a small bias towards larger variances, with the smallest and largest biases exhibited for $\mathbf{d}_{HVM}$ and $\mathbf{d}_M$, respectively. For I_y, the marginal KLD associated with $\mathbf{d}_H$ is well-above the others (Fig. 8b). The secondmost and thirdmost best performing data set for this parameter are $\mathbf{d}_{HV}$ and $\mathbf{d}_{HVM}$, while $\mathbf{d}_M$ performs the poorest. The marginal KLDs

Table 2

KLDs and mean relative biases of $\mathbf{m}_{\hat{s}}$ for the different conditioning data types. Columns 1 and 2 show the mean μ_{KLD} and standard deviation σ_{KLD} of the KLDs using the ensemble of hydraulic conductivity realizations. Column 3 shows the KLD values for the joint posterior PDFs using one realization of the conditioning data obtained from Fig. 4d–f and highlighted in Fig. 7a–c. The subsequent pairs of columns show the marginal KLD values and relative mean biases for the marginal posteriors of each component of $\mathbf{m}_2$ using this specific realization.

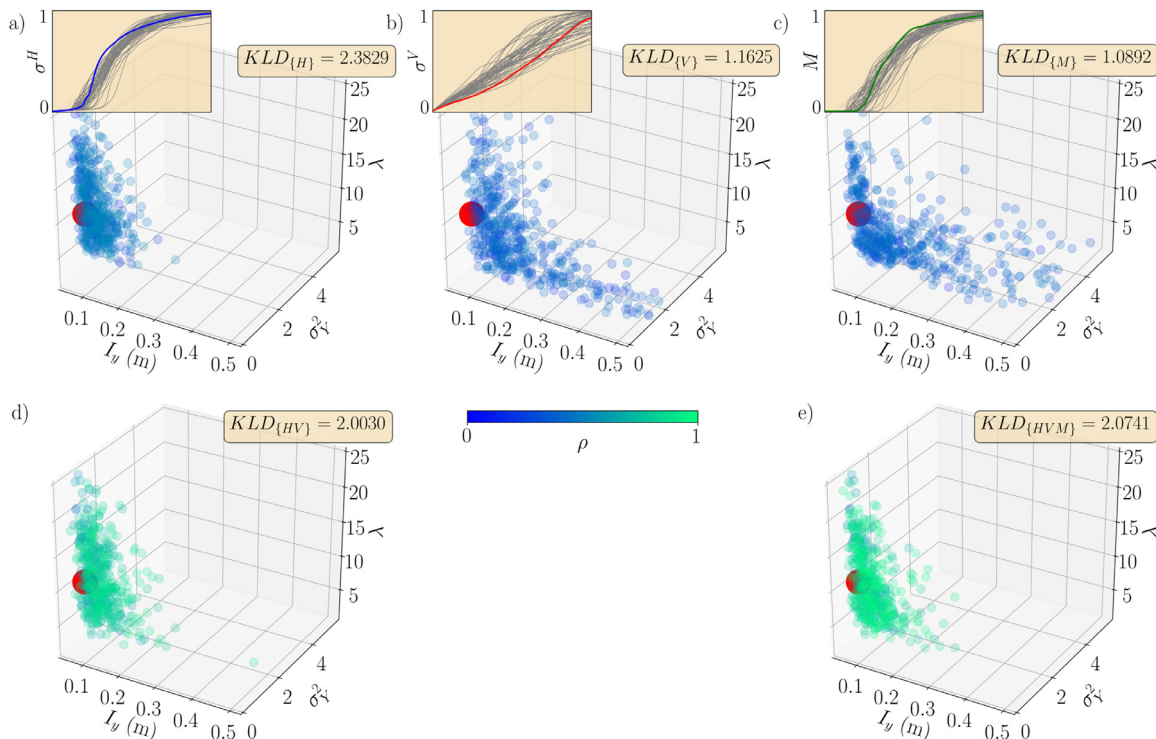|	Ensemble		$\mathbf{m}$	σ_Y^2		I_y (m)		λ	
	μ_{KLD}	σ_{KLD}	KLD	KLD	Bias	KLD	Bias	KLD	Bias
$\mathbf{d}_H$	2.1341	0.5027	2.3829	1.3179	0.3687	0.8065	0.0573	0.5979	0.0971
$\mathbf{d}_V$	1.4448	0.4425	1.1625	0.7427	0.4359	0.1115	0.6425	0.1003	0.7639
$\mathbf{d}_M$	1.3897	0.4768	1.0892	0.4866	0.4889	0.0875	0.6883	0.0952	0.8219
$\mathbf{d}_{HV}$	2.1114	0.4465	2.0030	0.9984	0.3019	0.6399	0.1306	0.5412	0.1657
$\mathbf{d}_{HVM}$	2.2256	0.4648	2.0741	1.0955	0.2452	0.6158	0.1417	0.4410	0.2640

Fig. 7. Posterior model parameter vector samples of size $S = 500$ obtained by the AARS algorithm for test case $\mathbf{m}_2 = (0.80, 0.06\,\text{m}, 10.00)$ using different datasets as conditioning data. The colored clouds of points represent the samples for datasets (a) $\mathbf{d}_H$; (b) $\mathbf{d}_V$; (c) $\mathbf{d}_M$; (d) $\mathbf{d}_{HV}$; (e) $\mathbf{d}_{VM}$; (f) $\mathbf{d}_{HVM}$. The colormap encodes the L_1 distance ρ between simulated and observed data, normalized by the minimum and maximum values of ρ of the test case. The inset plots of (a), (b) and (c) show, respectively, the 50 realizations of time-series σ^H, σ^V and M generated for $\mathbf{m}_1$ using different $\mathbf{R}$-realizations. The data considered here for inference are shown by thick-colored curves. The resulting KLD values are given for each dataset.

and biases for λ (Fig. 8b) follow the ranking of I_y. For this test case $\mathbf{m}_2$, the data better constrain the geostatistical parameters than for test case $\mathbf{m}_1$ as reflected by generally much larger KLD values.

4.3.3. Test case $\mathbf{m}_3$

Table 3 summarizes the performance of the different datasets for test case $\mathbf{m}_3$.

Considering the ensemble statistics of the joint posterior KLDs, we find that $\mathbf{d}_{HV}$ has the largest mean KLD, closely followed by $\mathbf{d}_{HVM}$ and $\mathbf{d}_H$. Again, $\mathbf{d}_M$ features the smallest mean KLD with a values that is $\sim 63\%$ of that for $\mathbf{d}_{HV}$. The standard deviations are varying within $\sim 15\%$ and represent $\sim 25\%$ of the mean values.

We now consider the results from the data time-series (Fig. 9a–c) obtained from the fields in Figs. 4g–i. The joint KLD for $\mathbf{d}_H$ is the largest closely followed by $\mathbf{d}_{HV}$ and $\mathbf{d}_{HVM}$. Their KLDs are $\sim 30\%$ higher than the others. The point clouds of posterior model realizations (Fig. 9) are

rather similar, but the results obtained from $\mathbf{d}_H$ (Fig. 9a) are more compact compared to $\mathbf{d}_V$ and $\mathbf{d}_M$. For instance there is minimal scatter in the λ-direction (c.f., Fig. 9b) and the high σ_Y^2 is better constrained (c.f. Fig. 9c).

The marginal KLDs are again the highest for σ_Y^2 followed by I_y and λ. The relative mean biases show a similar trend, being smallest for σ_Y^2. The marginal probability densities for σ_Y^2 (Fig. 10a) show that $\mathbf{d}_H$ best constrain this parameter, followed by $\mathbf{d}_{HV}$ and $\mathbf{d}_{HVM}$. The marginal KLD for $\mathbf{d}_H$ are only $\sim 10\%$ larger than for $\mathbf{d}_{HV}$ and $\mathbf{d}_{HVM}$, but its bias is 30% lower. Note also that $\mathbf{d}_M$ is strongly biased towards too low σ_Y^2. For I_y and λ, both KLDs and biases indicate that $\mathbf{d}_H$, $\mathbf{d}_{HV}$ and $\mathbf{d}_{HVM}$ are the most informative, while $\mathbf{d}_V$ has the poorest performance.
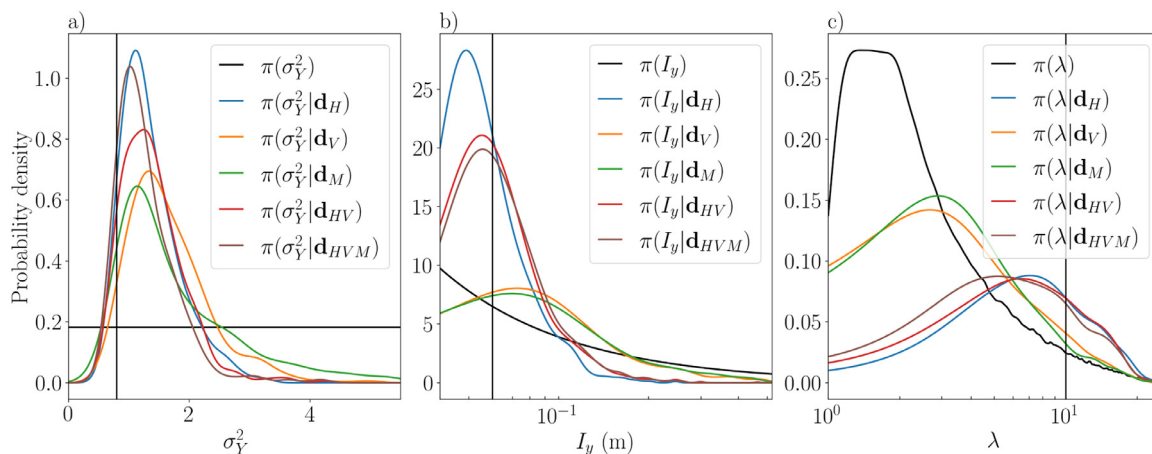
Fig. 8. (Color online) Marginal posterior PDFs associated to each type of conditioning data $\mathbf{d}_H$, $\mathbf{d}_V$, $\mathbf{d}_M$, $\mathbf{d}_{HV}$, $\mathbf{d}_{VM}$ and $\mathbf{d}_{HVM}$ for test case $\mathbf{m}_2 = (0.80, 0.06\,\text{m}, 10.00)$. Marginal prior and posterior PDFs corresponding to (a) σ_Y^2 (b) I_y and (c) λ.

Table 3
KLDs and mean relative biases of $\mathbf{m}_{\tilde{y}}$ for the different conditioning data types. Columns 1 and 2 show the mean μ_{KLD} and standard deviation σ_{KLD} of the KLDs using the ensemble of hydraulic conductivity realizations. Column 3 shows the KLD values for the joint posterior PDFs using one realization of the conditioning data obtained from Figs. 4g–i and highlighted in Fig. 9a–c. The subsequent pairs of columns show the marginal KLD values and relative mean biases for the marginal posteriors of each component of $\mathbf{m}_3$ using this specific realization.

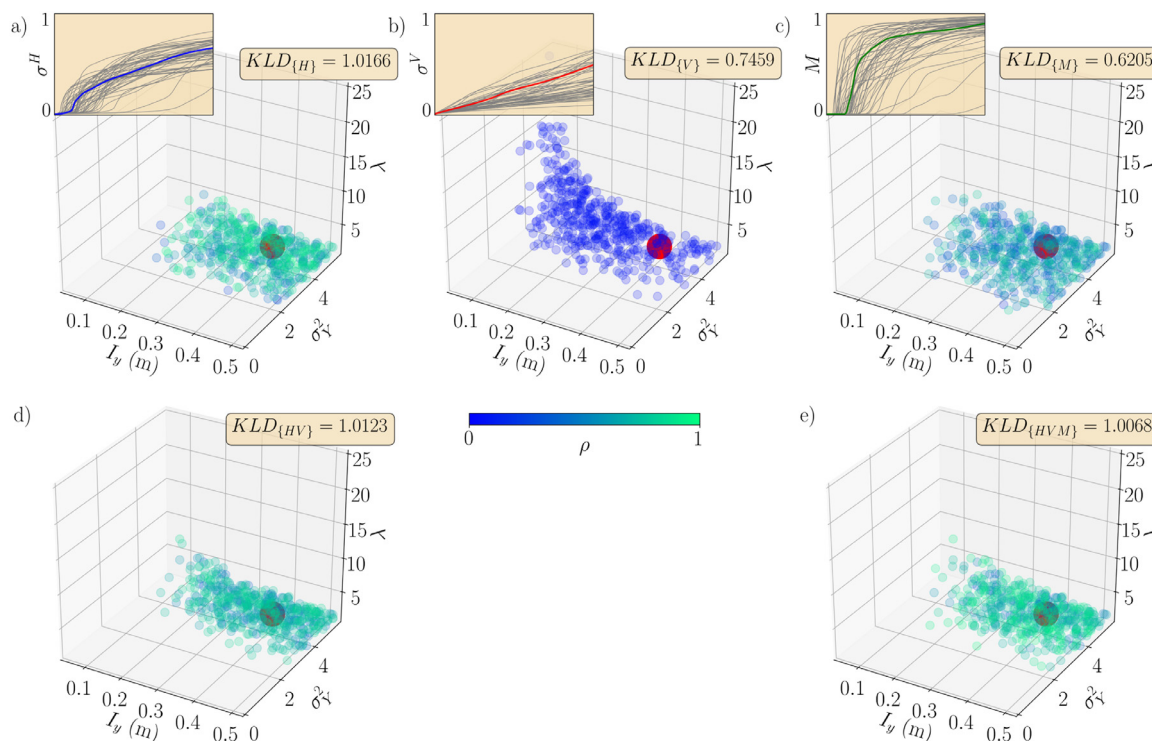|	Ensemble		$\mathbf{m}$	σ_Y^2		$I_y\,(\text{m})$		λ	
	μ_{KLD}	σ_{KLD}	KLD	KLD	Bias	KLD	Bias	KLD	Bias
$\mathbf{d}_H$	1.1845	0.3195	1.0166	0.4818	0.3098	0.2681	0.6388	0.2031	0.3962
$\mathbf{d}_V$	1.0565	0.3313	0.7459	0.3046	0.6171	0.0488	0.9635	0.0356	1.0166
$\mathbf{d}_M$	0.8413	0.2798	0.6205	0.2019	0.7347	0.1949	0.6983	0.1296	0.5169
$\mathbf{d}_{HV}$	1.3462	0.3491	1.0123	0.4491	0.4202	0.2680	0.6577	0.2054	0.4002
$\mathbf{d}_{HVM}$	1.2932	0.3100	1.0068	0.4200	0.4429	0.2915	0.6164	0.2245	0.3647

Fig. 9. Posterior model parameter vector samples of size $S = 500$ obtained by the AARS algorithm for test case $\mathbf{m}_3 = (4.70, 0.38\,\text{m}, 1.50)$ using different datasets as conditioning data. The colored clouds of points represent the samples for datasets (a) $\mathbf{d}_H$; (b) $\mathbf{d}_V$; (c) $\mathbf{d}_M$; (d) $\mathbf{d}_{HV}$; (e) $\mathbf{d}_{VM}$; (f) $\mathbf{d}_{HVM}$. The colormap encodes the L_1 distance ρ between simulated and observed data, normalized by the minimum and maximum values of ρ of the test case. The inset plots of (a), (b) and (c) show, respectively, the 50 realizations of time-series σ^H, σ^V and M generated for $\mathbf{m}_1$ using different **R**-realizations. The data considered here for inference are shown by thick-colored curves. The resulting KLD values are given for each dataset.
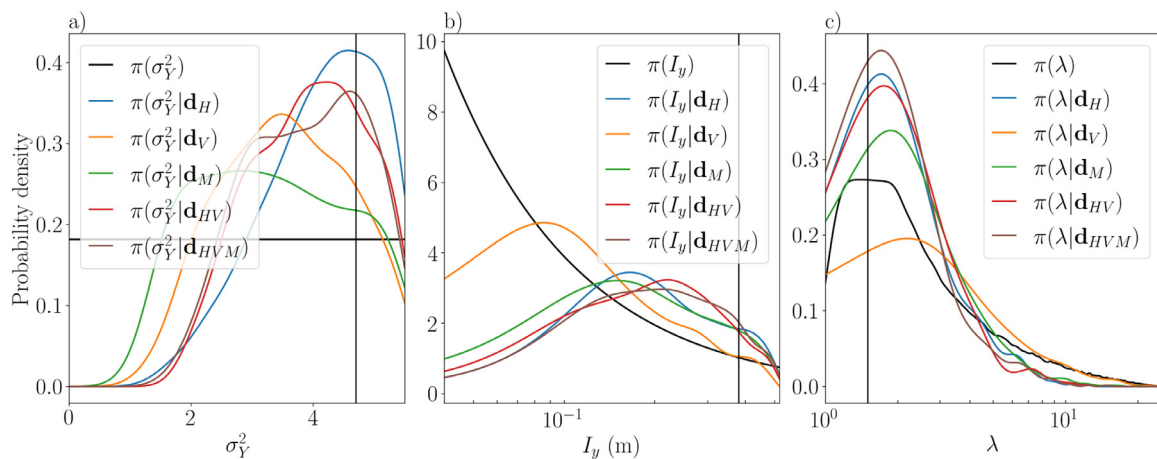
Fig. 10. (Color online) Marginal posterior PDFs associated to each type of conditioning data $\mathbf{d}_H$, $\mathbf{d}_V$, $\mathbf{d}_M$, $\mathbf{d}_{HV}$, $\mathbf{d}_{VM}$ and $\mathbf{d}_{HVM}$ for test case $\mathbf{m}_3 = (4.7, 0.38\,\mathrm{m}, 1.5)$. Marginal prior and posterior PDFs corresponding to (a) σ_Y^2 (b) I_y and (c) λ.

5. Discussion

5.1. General findings

The absolute values of the computed KLDs and biases are dependent on the choices made when approximating the posterior probability densities (Section 2.2), such as the width of the acceptance kernel of the AARS algorithm (Algorithm 2) and the bandwidth of the kernel density function used to represent the probability densities. For this reason, we focus our discussion below on relative differences between datasets and test cases. We first summarize the main results that apply to all test cases before discussing the test cases one-by-one. After this, we discuss broader implications of this research.

Considering the ensemble statistics of 50 hydraulic conductivity realizations for each test case, we find that the information content of $\mathbf{d}_H$ measured by the KLD is higher than $\mathbf{d}_V$, which in turn is higher than $\mathbf{d}_M$ for the three test cases considered: $\mathbf{m}_1$ (Table 1), $\mathbf{m}_2$ (Table 2) and $\mathbf{m}_3$ (Table 3). The added value of combining different data types ($\mathbf{d}_{HV}$ and $\mathbf{d}_{HVM}$) is generally found to be comparatively low. When considering individual hydraulic conductivity realizations and associated fields (Fig. 4), we generally obtain relative rankings of the different data types that are consistent with those of the ensemble means. Given that we consider non-ergodic model domains, the actual locations of high- and low hydraulic conductivities governed by the nuisance variable $\mathbf{R}$ plays an important role in the data-generating process. Its impact is manifested by the comparatively high standard deviations of the KLD estimates (Tables 1–3) and (in the variability of the generated time-series (Figs. 5a–c, 7a–c and 9a–c). Despite this inherent stochastic variability, we consistently find that the best constrained parameter is σ_Y^2, followed by I_y and λ. The individual test cases are discussed in detail below.

5.2. Lessons learned from the three test cases

Test case $\mathbf{m}_1$ features a highly heterogeneous field $K(\mathbf{x})$ with relatively small structures (Fig. 4a), for which one could possibly assume that ergodic conditions are fullfilled and consequently that the geostatistical parameters are well-represented within the modelling domain, yet it corresponds to the least-constrained test case. Indeed, the $\mathbf{R}$-realization plays here a very important role, implying a rather weak mapping from the time-series to the geostatistical parameters of interest. To understand this, note first that $\{\sigma^H\}$ and $\{\sigma^V\}$ are only sensitive to the underlying geostatistical parameters through the solute spreading patterns that these parameters induce. Indeed, the electrical responses result from optimal current patterns established throughout the highly

non-ergodic and time-evolving distribution of local concentrations (i.e., conductivities) that are, in turn, driven by the flow field $\mathbf{q}(\mathbf{x})$. As in the example in Fig. 2, the hydraulic conductivity field $K(\mathbf{x})$ has small-scale structures and is close to isotropic (Fig. 4a) but its associated flow field $\mathbf{q}(\mathbf{x})$ exhibits pronounced channeling (Fig. 4b). This tendency of the flow field to concentrate in preferential flow channels for high σ_Y^2 is well-known (e.g. Cvetkovic et al., 1996). Hence, an ergodic $K(\mathbf{x})$ is no guarantee of well-sensed geostatistical parameters when using geoelectrically monitored saline tracer tests. Nevertheless, compared to the prior, the estimated marginal posterior densities suggest that the geostatistical model that needs a comparatively high σ_Y^2 (Fig. 6a) and very small or high I_y (Fig. 6b) are unlikely.

Test case $\mathbf{m}_2$ corresponds to a layered distribution of hydraulic conductivity with a moderate σ_Y^2. The KLDs (Table 2), and consequently the constraining nature of the time-series, are much higher than for test cases $\mathbf{m}_1$ (Table 1) and $\mathbf{m}_3$ (Table 3). For $\mathbf{m}_2$, the smallest variations between the $\mathbf{R}$-realizations are observed (Fig. 7a–c) since the actual location of the flow channels is of secondary importance in the data-generating process. The hydraulic conductivity field (Fig. 4d) and its associated flow field (Fig. 4e) are visually more similar to each other than for $\mathbf{m}_1$. This is a consequence of the large anisotropy factor imposing horizontally continuous structures within which the flow-field channels are naturally developed. Both $\{\sigma^H\}$ and $\{M\}$ are highly sensitive to the arrival of horizontal connections that are established by the solute when it arrives to the outlet. Considering the marginal KLDs, we find that high and low σ_Y^2-values are incompatible with the data (Fig. 8a), as is large I_y. For this test case $\mathbf{m}_2$, λ is particularly interesting as its true value is high and, therefore, of low prior probability (Fig. 8c). We see a strong ability of all time-series including $\{\sigma^H\}$ to constrain this parameter.

Test case $\mathbf{m}_3$ is a highly heterogeneous test case that distinguishes itself from $\mathbf{m}_1$ by its larger I_y. A consequence of the resulting larger structures is that the generated data vary widely between the different hydraulic conductivity realizations (see insets in Fig. 9a–c). Yet the KLDs (Table 3) are higher than for test case $\mathbf{m}_1$. Considering the marginal posterior PDFs, all datasets indicate that the underlying geostatistical model has a high σ_Y^2 (Fig. 10a), at least a moderately high I_y (Fig. 10b) and (that the field is close to isotropic (Fig. 10c).

5.3. Physical insights and open questions

In our idealized numerical investigation, we found consistently that geoelectrical data performed better than mass breakthrough data in constraining the geostatistical parameters. This is a consequence of the fact that, for a given geostatistical model, the actual positioning of high- and
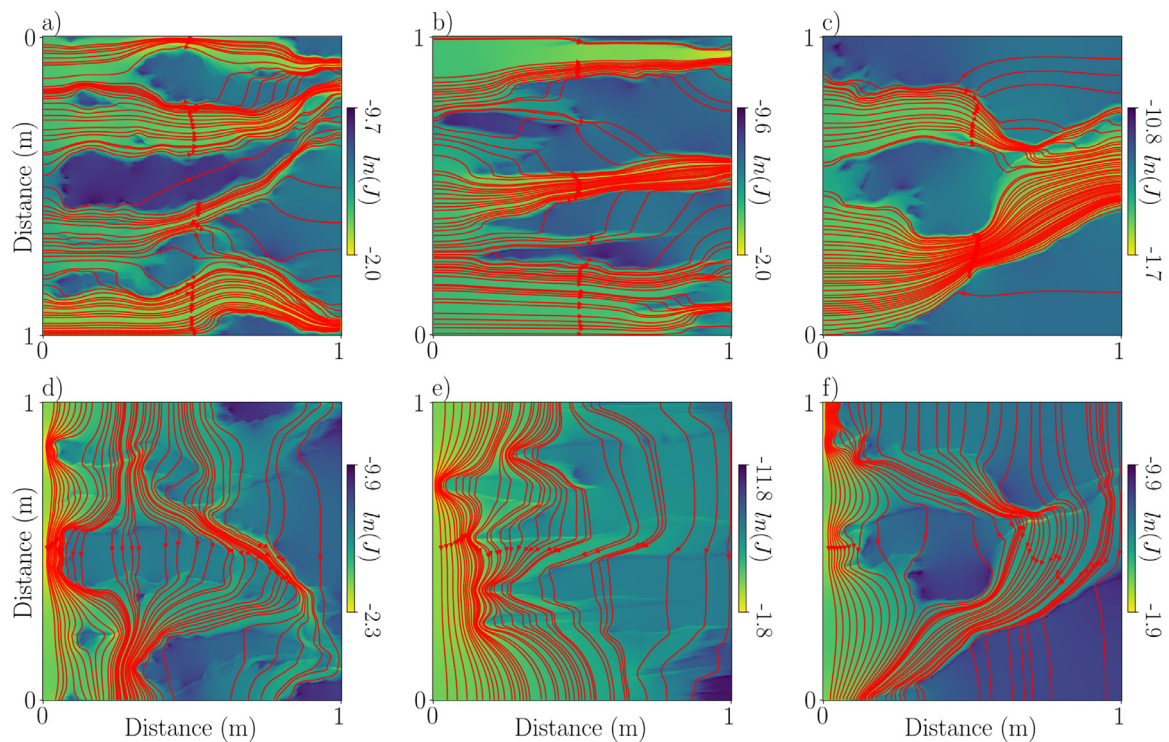
Fig. 11. Natural logarithm of the absolute value of the current density fields (and their streamlines) resulting from exciting the sample both in the (a–c) horizontal and (d–f) vertical modes. The electrical conductivity distribution is given by the saline concentration fields shown in Fig. 4, that is, at time 10^3 s for the three evaluated test cases (a, d) $\mathbf{m}_1$ (column 1), (b, e) $\mathbf{m}_2$ and (c, f) $\mathbf{m}_3$.

low hydraulic conductivity fields, governed by the nuisance variable **R**, has a larger impact on the mass breakthrough data than on the geoelectrical data (e.g., compare the insets in Fig. 9a–c). We understand this as a consequence of the local flux-averaged nature of the tracer breakthrough, compared to the more integrative non-linear volume-averaging of the electrical responses over the concentration field. Additionally, since $\{M\}$ is only sensitive to the time-evolution of the solute concentration field at the outlet, it cannot determine the causality of the arrival times, that is, if they originate from large horizontal correlation scales or from high variance, for instance.

We also found that $\{\sigma^H\}$ always has a higher constraining power than $\{\sigma^V\}$. This can be understood by noting that $\{\sigma^H\}$ is sensitive to electrical conduction paths created by the concentration field in the flow direction, leading to a very strong sensitivity to tracer arrivals at the outlet (e.g., Fig. 2e, or the generally steep slopes in the generated time-series in the insets of Figs. 5a, 7a and 9a). In Fig. 11 we plot the generated current density distributions determining $\{\sigma^H\}$ and $\{\sigma^V\}$ for the concentration fields shown in Figs. 4c, f and j. We see that for $\{\sigma^H\}$ (Figs. 11a–c) the support of the current density field (i.e. the regions of high current flow) is almost coincident with the area occupied by the invading tracer driven by the flow-field. This does not occur for $\{\sigma^V\}$ (Figs. 11d-f), indicating why $\{\sigma^H\}$ is more informative than $\{\sigma^V\}$. Clearly, $\{\sigma^V\}$ results from current patterns that are mainly constrained by vertical connection bottlenecks that become more common further away from the inlet region. This can be appreciated by the high density of current field streamlines observed at the inlet regions in Figs. 11d, 11e and 11f. This suggests that the main ability of $\{\sigma^V\}$ to sense the geostatistical parameters is through its sensitivity to the trailing end of the tracer front. Again, it is the connectivity-aspect of the electrical data that is at play.

Our results also suggest a strong dependence on the injection type. For a pulse injection, we expect $\{\sigma^H\}$ to be much less informative, compared to the present continuous injection case, as there will be no horizontal connections of salinity to sense. That is, the connectivity cre-

ated by establishing a continuous concentration field across the domain is very helpful for electrical-based inference of geostatistical properties from tracer tests.

For all test cases, we find that σ_Y^2 is the best constrained parameter. This is explained by the fact that σ_Y^2 controls the spreading rate of the solute (e.g., Gelhar and Axness, 1983) and is, thus, a first-order feature of the time-series. It will determine the time-spacing or pace of occurrence of the horizontal connection events as sensed particularly well by $\{\sigma^H\}$. However, also the trailing part of the tracer field as sensed by $\{\sigma^V\}$ is affected by σ_Y^2.

One open question is to what extent the electrical data can constrain mixing and spreading. Intuitively, there should be a strong sensitivity to the spreading width as σ^H is highly sensitive to the front of the tracer plume and σ^V to its end. Since solute spreading ultimately controls solute mixing (e.g., Villermaux, 2019), the high sensitivity of the electrical data to the former indicates that these data are able to at least quantify the mixing potential of the solute (e.g., de Dreuzy et al., 2012). This will be the topic of future research. Furthermore, the equivalent electrical conductivity tensor time-series is determined by the time-evolution of the concentration field, which in turn is driven by the flow-field. This suggests that that the electrical data might be more strongly related with the flow-field than the geostatistical model of log-hydraulic conductivity. In the future, we plan to study the geoelectrical sensitivity to flow-field descriptors (e.g., Koponen et al., 1996; Englert et al., 2006). Similarly, we would like to relate the electrical data to concentration field descriptors. However, as the concentration field is time-variant, this is more challenging to summarize than the steady-state flow field. One possibility is to relate it to the spatial distribution of localized temporal moments of the solute concentration field (Cirpka and Kitanidis, 2000).

5.4. Implications for field-based studies

Our work has several implications for field-based and laboratory-based electrical time-lapse monitoring of tracer tests. The first is that

ignoring significant tracer-concentration heterogeneity below a given scale will tend to underestimate mass when interpreting tomograms (Fig. 3d) and bias inferred transport parameters when performing a fully-coupled hydrogeophysical inversion. This can be circumvented through appropriate geostatistics-based time-lapse hydrogeophysical inversions (e.g., Kowalsky et al., 2005) provided that overly simple model parameterizations are avoided (Hinnell et al., 2010). Furthermore, we demonstrate for non-ergodic situations, common to many hydrogeophysically-monitored tracer tests, that both the locations of high- and low hydraulic conductivities (in our case controlled by **R**) and the geostatistical model have a strong impact on the measured data, suggesting that inversion approaches should attempt to constrain both of these aspects (Laloy et al., 2015). Our results suggest that for a well-designed time-lapse experiment, it might be possible to infer geostatistical parameters with relatively few measurement configurations, that is, without the need to actually resolve the tracer plume. Indeed, all the inferences performed in this study are based on upscaled equivalent values at the scale of the experiment. Another implication is that strong geoelectrical responses are mainly linked to preferential current pathways that in clay free formations are dependent on a near-continuous high-salinity region between the current electrodes. This suggests that continuous (compared to pulse) injections are preferable and that it could be beneficial to favor measurement configurations with one of the current electrodes located in the tracer source region (i.e., in the pit in which injection is performed or in a packed-off injection interval in a borehole). It also suggests that using push-pull technology for electrode installations, thereby allowing for more of a 3-D localization of electrodes without associated borehole effects (Doetsch et al., 2010) and costly boreholes, could enable improved imaging by allowing the tracer to arrive to the electrodes (Pidlisecky et al., 2006). Furthermore, unaccounted saline tracer heterogeneity should lead to anisotropic behavior at larger scales. For instance, when interpreting crosshole time-lapse data with two boreholes using so-called AB-MN configurations (current and potential electrodes in different boreholes) leading to mainly vertical current patterns or AM-BN configurations (one current and potential eletrode in each borehole) leading to mainly horizontal current patterns (Bing and Greenhalgh, 2001), then it might be essential to account for anisotropy in the inversion to avoid inversion artifacts (Herwanger et al., 2004). Furthermore, we expect that any inferred upscaled anisotropy measures such as anisotropy factors could guide the interpretation about the spatial organization of the concentration field below the resolution scale of the resulting tomograms (e.g., different behaviors of $\{\sigma^H\}$ and $\{\sigma^V\}$ in Fig. 3d).

6. Conclusions

We use Approximate Bayesian Computation to assess to what extent equivalent electrical conductivity time-series associated with tracer tests constrain geostatistical parameters governing small-scale structure. We consider an idealized set-up in which local concentration and electrical conductivity is linearly and perfectly correlated, implying that the results correspond to a best-case scenario. By considering three different geostatistical test models and ensemble statistics of 50 corresponding hydraulic conductivity field realizations, we find that $\{\sigma^H\}$ is the most informative data type, followed by $\{\sigma^V\}$ and $\{M\}$. The added value of combining different time-series is comparatively low. We further find that σ_Y^2 is the best-constrained geostatistical parameter followed by I_y and λ. The geostatistical parameters are the best constrained when considering data generated with a large λ. Ignoring concentration heterogeneity (i.e., assuming well-mixed conditions below a given scale) leads to underestimated solute mass when interpreting electrical data. This is a consequence of non-linear averaging and suggests that hydrogeophysical data interpretations and coupled hydrogeophysical inversions need to consider highly resolved hydraulic conductivity, fluid flow, concentration and electrical simulations in order to avoid biased results. Casting the inference problem within a geostatistical framework decreases

the number of electrical configurations needed to constrain the geostatistical parameters. Since the electrical data are primarily sensitive to the presence (or not) of a connected high-concentration field between current electrodes, we recommend experimental setups favoring continuous tracer injections including measurement configurations with one electrode located within the tracer injection area.

Declaration of Competing Interest

The authors declare that they have no known competing financial interests or personal relationships that could have appeared to influence the work reported in this paper.

CRediT authorship contribution statement

Alejandro Fernandez Visentini: Writing - original draft, Writing - review & editing, Methodology, Conceptualization, Software, Formal analysis, Investigation. **Niklas Linde:** Conceptualization, Methodology, Supervision, Writing - original draft, Writing - review & editing. **Tanguy Le Borgne:** Writing - review & editing, Conceptualization. **Marco Dentz:** Writing - review & editing, Conceptualization.

Acknowledgments

References

Archie, G.E., 1942. The electrical resistivity log as an aid in determining some reservoir characteristics. Trans. AIME 146 (01), 54–62. https://doi.org/10.2118/942054-G.

Beaumont, M.A., Zhang, W., Balding, D.J., 2002. Approximate Bayesian computation in population genetics. Genetics 162 (4), 2025–2035.

Bedekar, V., Morway, E.D., Langevin, C.D., Tonkin, M.J., 2016. MT3D-USGS version 1: A US Geological Survey Release of MT3DMS Updated with New and Expanded Transport Capabilities for use with MODFLOW. Technical Report. US Geological Survey. https://doi.org/10.3133/tm6A53.

Bernabé, Y., Revil, A., 1995. Pore-scale heterogeneity, energy dissipation and the transport properties of rocks. Geophys. Res. Lett. 22 (12), 1529–1532. https://doi.org/10.1029/95GL01418.

Bing, Z., Greenhalgh, S., 2001. Cross-hole resistivity tomography using different electrode configurations. Geophys. Prospect. 48 (5), 887–912. https://doi.org/10.1046/j.1365-2478.2000.00220.x.

Binley, A., Cassiani, G., Middleton, R., Winship, P., 2002. Vadose zone flow model parameterisation using cross-borehole radar and resistivity imaging. J. Hydrol. 267 (3–4), 147–159. https://doi.org/10.1016/S0022-1694(02)00146-4.

Binley, A., Hubbard, S.S., Huisman, J.A., Revil, A., Robinson, D.A., Singha, K., Slater, L.D., 2015. The emergence of hydrogeophysics for improved understanding of subsurface processes over multiple scales. Water Resour. Res. 51 (6), 3837–3866. https://doi.org/10.1002/2015WR017016.

Budka, M., Gabrys, B., Musial, K., 2011. On accuracy of pdf divergence estimators and their applicability to representative data sampling. Entropy 13 (7), 1229–1266. https://doi.org/10.3390/e13071229.

Cirpka, O.A., Kitanidis, P.K., 2000. Characterization of mixing and dilution in heterogeneous aquifers by means of local temporal moments. Water Resour. Res. 36 (5), 1221–1236. https://doi.org/10.1029/1999WR900354.

Cover, T.M., Thomas, J.A., 2012. Elements of Information Theory. John Wiley & Sons.

Cox, R.A., Nishikawa, T., 1991. A new total variation diminishing scheme for the solution of advective-dominant solute transport. Water Resour. Res. 27 (10), 2645–2654. https://doi.org/10.1029/91WR01746.

Curtis, A., Lomax, A., 2001. Prior information, sampling distributions, and the curse of dimensionality. Geophysics 66 (2), 372–378. https://doi.org/10.1190/1.1444928.

Cvetkovic, V., Cheng, H., Wen, X.-H., 1996. Analysis of nonlinear effects on tracer migration in heterogeneous aquifers using Lagrangian travel time statistics. Water Resour. Res. 32 (6), 1671–1680. https://doi.org/10.1029/96WR00278.

Daily, W., Ramirez, A., LaBrecque, D., Nitao, J., 1992. Electrical resistivity tomography of vadose water movement. Water Resour. Res. 28 (5), 1429–1442. https://doi.org/10.1029/91WR03087.

Day-Lewis, F.D., Singha, K., Binley, A.M., 2005. Applying petrophysical models to radar travel time and electrical resistivity tomograms: resolution-dependent limitations. J. Geophys. Res. 110 (B8). https://doi.org/10.1029/2004JB003569.

Dietrich, C.R., Newsam, G.N., 1997. Fast and exact simulation of stationary Gaussian processes through circulant embedding of the covariance matrix. SIAM J. Sci. Comput. 18, 1088–1107. https://doi.org/10.1137/S1064827592240555.

Doetsch, J.A., Coscia, I., Greenhalgh, S., Linde, N., Green, A., Günther, T., 2010. The borehole-fluid effect in electrical resistivity imaging. Geophysics 75 (4), F107–F114. https://doi.org/10.1190/1.3467824.

de Dreuzy, J.-R., Carrera, J., Dentz, M., Le Borgne, T., 2012. Time evolution of mixing in heterogeneous porous media. Water Resour. Res. 48 (6). https://doi.org/10.1029/2011WR011360.

Englert, A., Vanderborght, J., Vereecken, H., 2006. Prediction of velocity statistics in three-dimensional multi-Gaussian hydraulic conductivity fields. Water Resour. Res. 42 (3). https://doi.org/10.1029/2005WR004014.

Feynman, R.P., Leighton, R.B., Sands, M., 2011. The Feynman Lectures on Physics, Vol. I: The New Millennium Edition: Mainly Mechanics, Radiation, and Heat, 1. Basic Books.

Fowler, D.E., Moysey, S.M., 2011. Estimation of aquifer transport parameters from resistivity monitoring data within a coupled inversion framework. J. Hydrol. 409 (1–2), 545–554. https://doi.org/10.1016/j.jhydrol.2011.08.063.

Friedel, S., 2003. Resolution, stability and efficiency of resistivity tomography estimated from a generalized inverse approach. Geophys. J. Int. 153 (2), 305–316. https://doi.org/10.1046/j.1365-246X.2003.01890.x.

Gelhar, L.W., Axness, C.L., 1983. Three-dimensional stochastic analysis of macrodispersion in aquifers. Water Resour. Res. 19 (1), 161–180. https://doi.org/10.1029/WR019i001p00161.

Gelman, A., Carlin, J.B., Stern, H.S., Dunson, D.B., Vehtari, A., Rubin, D.B., 2013. Bayesian Data Analysis. CRC Press.

Harbaugh, A.W., 2005. MODFLOW-2005, the US Geological Survey Modular Ground-Water Model: the Ground-Water Flow Process. US Department of the Interior, US Geological Survey Reston, VA. https://doi.org/10.3133/tm6A16.

Herwanger, J., Pain, C., Binley, A., De Oliveira, C., Worthington, M., 2004. Anisotropic resistivity tomography. Geophys. J. Int. 158 (2), 409–425. https://doi.org/10.1111/j.1365-246X.2004.02314.x.

Hill, M.C., 1990. Solving groundwater flow problems by conjugate-gradient methods and the strongly implicit procedure. Water Resour. Res. 26 (9), 1961–1969. https://doi.org/10.1029/WR026i009p01961.

Hill, R., 1963. Elastic properties of reinforced solids: some theoretical principles. J. Mech. Phys. Solids 11 (5), 357–372. https://doi.org/10.1016/0022-5096(63)90036-X.

Hinnell, A., Ferré, T., Vrugt, J., Huisman, J., Moysey, S., Rings, J., Kowalsky, M., 2010. Improved extraction of hydrologic information from geophysical data through coupled hydrogeophysical inversion. Water Resour. Res. 46 (4). https://doi.org/10.1029/2008WR007060.

Jougnot, D., Jiménez-Martínez, J., Legendre, R., Le Borgne, T., Méheust, Y., Linde, N., 2018. Impact of small-scale saline tracer heterogeneity on electrical resistivity monitoring in fully and partially saturated porous media: insights from geoelectrical milli-fluidic experiments. Adv. Water Resour. 113, 295–309. https://doi.org/10.1016/j.advwatres.2018.01.014.

Keller, G.V., Frischknecht, F.C., 1966. Electrical Methods in Geophysical Prospecting. Pergamon.

Kemna, A., Vanderborght, J., Kulessa, B., Vereecken, H., 2002. Imaging and characterisation of subsurface solute transport using electrical resistivity tomography (ERT) and equivalent transport models. J. Hydrol. 267 (3–4), 125–146. https://doi.org/10.1016/S0022-1694(02)00145-2.

Koestel, J., Kemna, A., Javaux, M., Binley, A., Vereecken, H., 2008. Quantitative imaging of solute transport in an unsaturated and undisturbed soil monolith with 3-D ERT and TDR. Water Resour. Res. 44 (12). https://doi.org/10.1029/2007WR006755.

Koponen, A., Kataja, M., Timonen, J.v., 1996. Tortuous flow in porous media. Phys. Rev. E 54 (1), 406. https://doi.org/10.1103/PhysRevE.54.406.

Kowalsky, M.B., Finsterle, S., Peterson, J., Hubbard, S., Rubin, Y., Majer, E., Ward, A., Gee, G., 2005. Estimation of field-scale soil hydraulic and dielectric parameters through joint inversion of GPR and hydrological data. Water Resour. Res. 41 (11). https://doi.org/10.1029/2005WR004237.

Kullback, S., Leibler, R.A., 1951. On information and sufficiency. Ann. Math. Stat. 22 (1), 79–86. https://doi.org/10.1214/aoms/1177729694.

Laloy, E., Linde, N., Jacques, D., Vrugt, J.A., 2015. Probabilistic inference of multi-Gaussian fields from indirect hydrological data using circulant embedding and dimensionality reduction. Water Resour. Res. 51 (6), 4224–4243. https://doi.org/10.1002/2014WR016395.

Laloy, E., Linde, N., Vrugt, J.A., 2012. Mass conservative three-dimensional water tracer distribution from Markov chain Monte Carlo inversion of time-lapse ground-penetrating radar data. Water Resour. Res. 48 (7). https://doi.org/10.1029/2011WR011238.

Lesmes, D.P., Friedman, S.P., 2005. Relationships between the electrical and hydrogeological properties of rocks and soils. In: Hydrogeophysics. Springer, pp. 87–128.

Li, Y., Oldenburg, D.W., 1991. Aspects of charge accumulation in dc resistivity experiments. Geophys. Prospect. 39 (6), 803–826. https://doi.org/10.1111/j.1365-2478.1991.tb00345.x.

Milton, G.W., Sawicki, A., 2003. Theory of composites. Cambridge monographs on applied and computational mathematics. Appl. Mech. Rev. 56 (2), B27–B28.

Mosegaard, K., Tarantola, A., 1995. Monte Carlo sampling of solutions to inverse problems. J. Geophys. Res. 100 (B7), 12431–12447. https://doi.org/10.1029/94JB03097.

Moysey, S., Singha, K., Knight, R., 2005. A framework for inferring field-scale rock physics relationships through numerical simulation. Geophys. Res. Lett. 32 (8). https://doi.org/10.1029/2004GL022152.

Nussbaumer, R., Linde, N., Mariethoz, G., Holliger, K., 2019. Simulation of fine-scale electrical conductivity fields using resolution-limited tomograms and area-to-point kriging. Geophys. J. Int. 218 (2), 1322–1335. https://doi.org/10.1093/gji/ggz185.

Ogata, A., Banks, R., 1961. A Solution of the Differential Equation of Longitudinal Dispersion in Porous Media: Fluid Movement in Earth Materials. US Government Printing Office. https://doi.org/10.3133/pp411A.

Pidlisecky, A., Knight, R., Haber, E., 2006. Cone-based electrical resistivity tomography. Geophysics 71 (4), G157–G167. https://doi.org/10.1190/1.2213205.

Pollock, D., Cirpka, O.A., 2012. Fully coupled hydrogeophysical inversion of a laboratory salt tracer experiment monitored by electrical resistivity tomography. Water Resour. Res. 48 (1). https://doi.org/10.1029/2011WR010779.

Rubin, Y., 2003. Applied Stochastic Hydrogeology. Oxford University Press.

Rücker, C., Günther, T., Wagner, F.M., 2017. pyGIMLi: an open-source library for modelling and inversion in geophysics. Comput. Geosci. 109, 106–123. https://doi.org/10.1016/j.cageo.2017.07.011.

Sanchez-Vila, X., Guadagnini, A., Carrera, J., 2006. Representative hydraulic conductivities in saturated groundwater flow. Rev. Geophys. 44 (3). https://doi.org/10.1029/2005RG000169.

Scales, J.A., 1996. Uncertainties in seismic inverse calculations. In: Inverse Methods. Springer, pp. 79–97.

Silverman, B.W., 1986. Density Estimation for Statistics and Data Analysis, 26. CRC Press.

Singha, K., Day-Lewis, F.D., Johnson, T., Slater, L.D., 2015. Advances in interpretation of subsurface processes with time-lapse electrical imaging. Hydrol. Process. 29 (6), 1549–1576. https://doi.org/10.1002/hyp.10280.

Singha, K., Gorelick, S.M., 2005. Saline tracer visualized with three-dimensional electrical resistivity tomography: field-scale spatial moment analysis. Water Resour. Res. 41 (5). https://doi.org/10.1029/2004WR003460.

Sisson, S., Fan, Y., Beaumont, M., 2018. Overview of ABC. Handb. Approx. Bayesian Comput. 3–54.

Slater, L., Binley, A., Daily, W., Johnson, R., 2000. Cross-hole electrical imaging of a controlled saline tracer injection. J. Appl. Geophy. 44 (2–3), 85–102. https://doi.org/10.1016/S0926-9851(00)00002-1.

Tarantola, A., 2005. Inverse Problem Theory and Methods for Model Parameter Estimation, 89. SIAM.

Vanderborght, J., Kemna, A., Hardelauf, H., Vereecken, H., 2005. Potential of electrical resistivity tomography to infer aquifer transport characteristics from tracer studies: a synthetic case study. Water Resour. Res. 41 (6). https://doi.org/10.1029/2004WR003774.

Villermaux, E., 2019. Mixing versus stirring. Annu. Rev. Fluid Mech. 51, 245–273. https://doi.org/10.1146/annurev-fluid-010518-040306.

Wand, M.P., Jones, M.C., 1994. Kernel Smoothing. CRC Press.